AD-A170 136 THE USE OF NOVEL PROCESSING PROCEDURES FOR IMPROVING 1/2
OVERALL FATIGUE RESI (U) VIRGINIA UNIV CHARLOTTESVILLE
DEPT OF MATERIALS SCIENCE E A STARKE APR 86
UNCLASSIFIED UVA/525644/MS86/101 AFOSR-TR-86-0492 F/G 11/6 NL

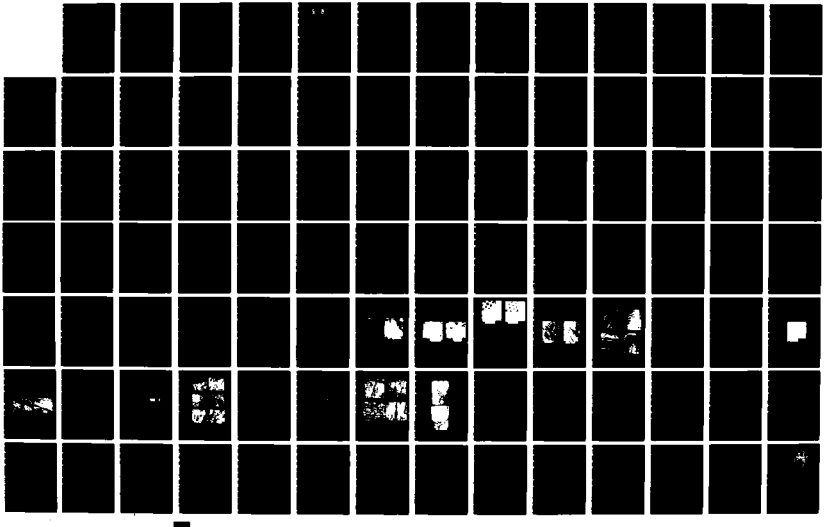

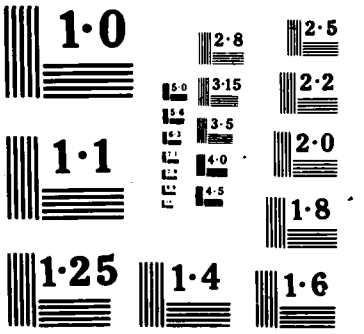
1·0
1·1
1·25
1·4
1·6
1·8
2·0
2·2
2·5
2·8
3·15
3·5
4·0
4·5
5·0

Annual Report

THE USE OF NOVEL PROCESSING PROCEDURES FOR IMPROVING OVERALL FATIGUE RESISTANCE OF HIGH STRENGTH ALUMINUM ALLOYS

Contract No. AFOSR-83-0061-C

Submitted to:

Air Force Office of Scientific Research/NE
Building 410
Bolling Air Force Base
Washington, D.C. 20332

Attention: Alan H. Rosenstein

Submitted by:

Edgar A. Starke, Jr.
Earnest Oglesby Professor and Dean

Report No. UVA/525644/MS86/101

April 1986

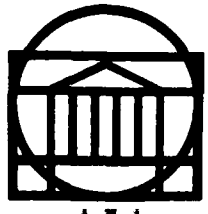

SCHOOL OF ENGINEERING AND APPLIED SCIENCE

DEPARTMENT OF MATERIALS SCIENCE

UNIVERSITY OF VIRGINIA
CHARLOTTESVILLE, VIRGINIA 22901

TABLE OF CONTENTS

Annual Report

THE USE OF NOVEL PROCESSING PROCEDURES FOR IMPROVING OVERALL FATIGUE RESISTANCE OF HIGH STRENGTH ALUMINUM ALLOYS

Submitted to:

Air Force Office of Scientific Research/NE
Building 410
Bolling Air Force Base
Washington, D.C. 20332

Attention: Alan H. Rosenstein

Submitted by:

Edgar A. Starke, Jr.
Earnest Oglesby Professor and Dean

Department of Materials Science
SCHOOL OF ENGINEERING AND APPLIED SCIENCE
UNIVERSITY OF VIRGINIA
CHARLOTTESVILLE, VIRGINIA

Report No. UVA/525644/MS86/101

April 1986

Copy No. ____

(2)

AD-A170 136

DTIC SELECTED JUL 25 1986 S D

REPORT DOCUMENTATION PAGE

1a. REPORT SECURITY CLASSIFICATION	1b. RESTRICTIVE MARKINGS
2a. SECURITY CLASSIFICATION AUTHORITY	3. DISTRIBUTION/AVAILABILITY OF REPORT: Approved for public release; distribution unlimited.
2b. DECLASSIFICATION/DOWNGRADING SCHEDULE	
4. PERFORMING ORGANIZATION REPORT NUMBER(S): UVA/525644/MS86/101	5. MONITORING ORGANIZATION REPORT NUMBER(S): AFOSR-TR- 86-0492
6a. NAME OF PERFORMING ORGANIZATION: University of Virginia; 6b. OFFICE SYMBOL (If applicable):	7a. NAME OF MONITORING ORGANIZATION: Air Force Office of Scientific Research/PDK
6c. ADDRESS (City, State and ZIP Code): Department of Materials Science, Thornton Hall, Charlottesville, VA 22901	7b. ADDRESS (City, State and ZIP Code): Building 410, Bolling Air Force Base, Washington, D.C. 20332-6448
8a. NAME OF FUNDING/SPONSORING ORGANIZATION: Air Force Office of Scientific Research/NE; 8b. OFFICE SYMBOL (If applicable): NE	9. PROCUREMENT INSTRUMENT IDENTIFICATION NUMBER: AFOSR-83-0061-C
8c. ADDRESS (City, State and ZIP Code): Building 410, Bolling Air Force Base, Washington, D.C. 20332-6448	10. SOURCE OF FUNDING NOS.

PROGRAM ELEMENT NO.	PROJECT NO.	TASK NO.	WORK UNIT NO.
61102F	2306	A1	

11. TITLE (Include Security Classification): USE OF NOVEL PROCESSING PROCEDURES

12. PERSONAL AUTHOR(S): Starke, E. A., Jr.

13a. TYPE OF REPORT	13b. TIME COVERED	14. DATE OF REPORT (Yr., Mo., Day)	15. PAGE COUNT
Annual	FROM 01/01/85 TO 12/31/85	1986 April 29	100

16. SUPPLEMENTARY NOTATION

17 COSATI CODES			18. SUBJECT TERMS (Continue on reverse if necessary and identify by block number)
FIELD	GROUP	SUB GR	

19. ABSTRACT (Continue on reverse if necessary and identify by block number)

This program was initiated on January 1, 1983. Its objective is to develop an understanding of the mechanisms involved in the initiation and propagation of cracks in metals in order to optimize the microstructure of high strength aluminum alloys for overall fracture resistance. The research conducted during this year was divided into three tasks.

Task I was concerned with the effects of slip character and grain size on the intrinsic material and extrinsic closure contributions to fatigue crack

20. DISTRIBUTION/AVAILABILITY OF ABSTRACT	21. ABSTRACT SECURITY CLASSIFICATION
UNCLASSIFIED/UNLIMITED ☐ SAME AS RPT ☐ DTIC USERS ☐	

22a. NAME OF RESPONSIBLE INDIVIDUAL	22b. TELEPHONE NUMBER (Include Area Code)	22c. OFFICE SYMBOL
Dr Alan H Rosenstein	202 767 4933	AFOSR/NE

DD FORM 1473, 83 APR EDITION OF 1 JAN 73 IS OBSOLETE

SECURITY CLASSIFICATION OF THIS PAGE

20. ABSTRACT (continued)

growth resistance of 7475. It involved the use of thermomechanical processing to modify the grain structure for enhancement of both intrinsic and extrinsic effects. In our last report we described the use of a direct current potential drop technique (DC-PD) to examine the possibility of crack tip welding in vacuum and the results of our initial experiments using this method. There were some problems with the analysis of the data and during the past year a method for an improved analysis was developed. This is described in detail in the report.

Task II was concerned with a study of the fatigue crack growth and fracture mechanisms of an Al-Li-Cu alloy. The experimental results were described in our last report along with a preliminary model which related the deformation behavior with the fracture toughness. During the past year we have refined our analysis and the model which accurately predicts the fracture toughness as a function of slip band spacing and width. This most recent work is discussed in the report.

Task III was concerned with secondary cracking in Al-Li-Cu, Al-Li-Mg and Al-Li-Cu-Mg alloys. Many recent studies of this class of alloys have shown that they can exhibit severe grain boundary cracking. The most commonly-observed manifestation of this cracking is the appearance of secondary cracks on fracture surfaces of tensile specimens loaded parallel to the rolling direction. We have identified four potential mechanisms for this cracking which include the effects of: (1) modulus, (2) segregation of Na and K to grain boundaries, (3) grain boundary precipitates, and (4) strain localization. We have designed experiments to examine each of these effects and our results to date are described in the report.

ABSTRACT

This program was initiated on January 1, 1983. Its objective is to develop an understanding of the mechanisms involved in the initiation and propagation of cracks in metals in order to optimize the microstructure of high strength aluminum alloys for overall fracture resistance. The research conducted during this year was divided into three tasks.

Task I was concerned with the effects of slip character and grain size on the intrinsic material and extrinsic closure contributions to fatigue crack growth resistance of 7475. It involved the use of thermomechanical processing to modify the grain structure for enhancement of both intrinsic and extrinsic effects. In our last report we described the use of a direct current potential drop technique (DC-PD) to examine the possibility of crack tip welding in vacuum and the results of our initial experiments using this method. There were some problems with the analysis of the data and during the past year a method for an improved analysis was developed. This is described in detail in the report.

Task II was concerned with a study of the fatigue crack growth and fracture mechanisms of an Al-Li-Cu alloy. The experimental results were described in our last report along with a preliminary model which related the deformation behavior with the fracture toughness. During the past year we have refined our analysis and the model which accurately predicts the fracture toughness as a function of slip band spacing and width. This most recent work is discussed in the report.

Task III was concerned with secondary cracking in Al-Li-Cu, Al-Li-Mg and Al-Li-Cu-Mg alloys. Many recent studies of this class of alloys have shown

that they can exhibit severe grain boundary cracking. The most commonly-observed manifestation of this cracking is the appearance of secondary cracks on fracture surfaces of tensile specimens loaded parallel to the rolling direction. We have identified four potential mechanisms for this cracking which include the effects of: (1) modulus, (2) segregation of Na and K to grain boundaries, (3) grain boundary precipitates, and (4) strain localization. We have designed experiments to examine each of these effects and our results to date are described in the report.

SUMMARY OF PROGRESS DURING 1985

TASK I. AN IMPROVED ANALYSIS OF THE POTENTIAL DROP METHOD FOR MEASURING CRACK LENGTHS IN COMPACT TENSION SPECIMENS

M. E. Orazem and W. W. Ruch

The measurement of an AC or DC potential drop across a region of local stress has become a standard method for determining the crack length in metal specimens (1-8). This technique provides a continuous and nondestructive determination of crack length; however, the interpretation of these data generally requires a separate calibration. For many specimen geometries, analytical solutions of Laplace's equation can be obtained which provide theoretical relationships among variables such as specimen geometry, measured potential drop, and crack lengths (9-12). Such analytical solutions can guide and support the calibration procedure, but are not available for the compact tension specimen geometry. Ritchie and Bathe (13) and Aronson and Ritchie (14) have obtained numerical solutions of Laplace's equation for the compact tension specimen through application of finite element analysis. Accurate use of finite element solutions of Laplace's equation for this system requires, however, a large number of nodes due to the singularities observed at the electrode edges. Orazem (15) has presented a numerical solution of Laplace's equation for this specimen geometry which alleviates this problem through use of conformal mapping coupled with a numerical technique. The objective of this work is to show the application of Orazem's results (15) to the potential drop method for compact tension specimens.

In practice, calibration curves are generally given in the form of V_a/V_{ao} versus a/W where V_a is the potential drop across a specimen with crack length a (see Figure 1) and V_{ao} is the reference potential drop for a specified value of a. Through the use of such nondimensional terms, the calibration curve

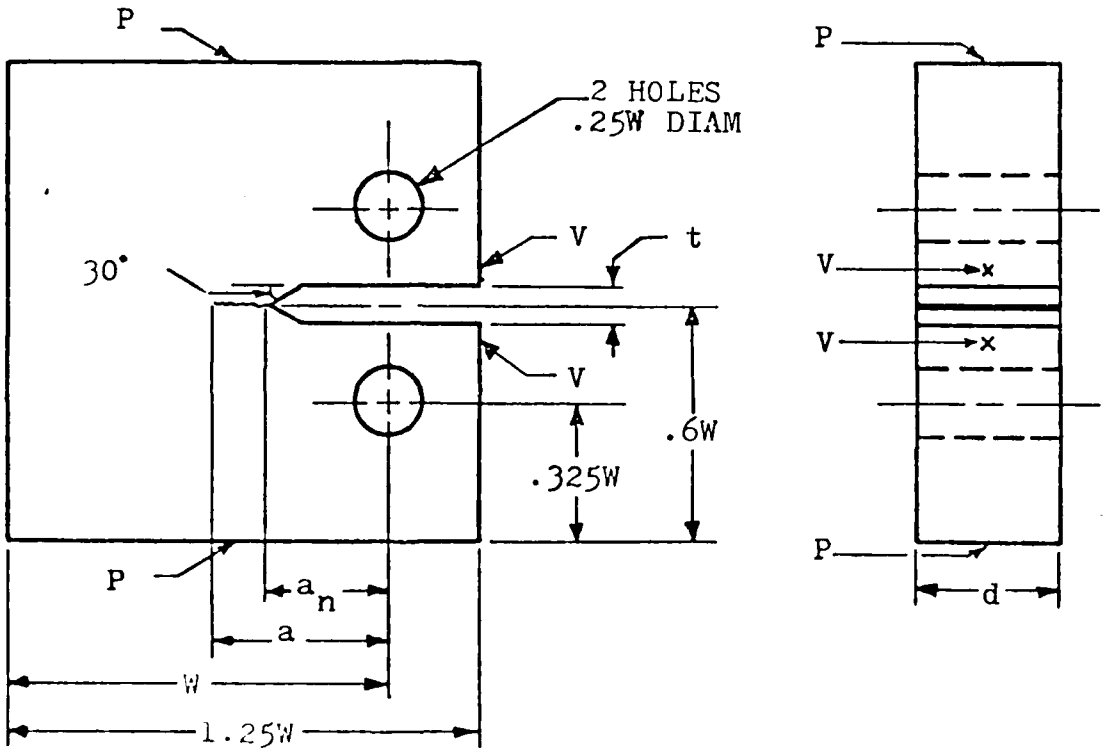

Figure 1. Schematic representation of a compact tension specimen. The locations of current inputs are represented by P, and the location of voltage measurement leads are represented by V.

becomes independent of the conductivity and thickness of the specimen and of the magnitude of the current. For a given specimen geometry, the calibration procedure involves obtaining an independent measure of the crack length through such methods as machining a crack to a specified depth, surface observation and measurement of the growing crack, marking the crack length by tinting or overloading, or use of an electrical analog, e.g., graphitized paper or aluminum foil where the crack length can be increased by cutting with a razor blade. The data obtained in this manner are then fit to a three parameter equation such as a power law model with the form

$$\frac{V_a}{V_{ao}} = C_1 + C_2 \left(\frac{a}{W}\right)^{C_3} \tag{1}$$

or a two parameter model such as

$$\frac{V_a}{V_{ao}} = C_1 \exp\left[\frac{1}{C_2}\left(\frac{a}{W} - \frac{a_o}{W}\right)\right] \tag{2}$$

where C_k are adjustable parameters obtained by a linear regression of the appropriate equation to the calibration data. These equations provide a good match to the calibration data but do not follow the correct asymptotic behavior at long crack lengths, a region where exact knowledge of the crack length is critical. Orazem (15) has suggested that the proper variable for this calibration is

$$\xi = (1 - a/W)\frac{W}{h} \tag{3a}$$

and the proper form for the calibration curve is

$$d\kappa R_1 = C_1 - \frac{4}{\pi} \ln(\xi) \tag{3b}$$

where $d\kappa R_1$ is the dimensionless resistance of the test specimen between the voltage probes related to the usual ratio of potential drop measurements by

$$d\kappa R_1 = \frac{V_a}{V_{ao}} V_{ao} \frac{d}{\rho I} \tag{3c}$$

These expressions are based upon the asymptotic solution for long crack lengths. With accurate measurement of the current I, the specimen thickness d, and the resistivity ρ, equation (3) provides an accurate form for the calibration curve with only one adjustable parameter. In addition, for the usual specimen geometry, this parameter is very close to zero. If the specimen resistivity is not known, equation (3) may be regarded to be a two parameter model from which a value for the specimen resistivity can be obtained.

While equation (3) provides the correct asymptotic solution for long crack lengths, the degree to which it applies to short crack lengths is perhaps surprising. The experimental verification of this approach is presented in this paper along with treatment of the conditions under which equation (3) does not apply. A brief discussion of the theoretical method is presented below. Readers interested in the application of these results may skip to the section Results and Discussion.

Theory

Primary current and potential distributions apply to systems for which the surface overpotential can be neglected and the phase adjacent to the electrode has a uniform potential. These assumptions are strictly valid for solid conductors in which the current is electronic. Calculation of the primary current and potential distributions involves solution of Laplace's equation, $\nabla^2 \phi = 0$, which is not trivial, even for simple geometries. The

method of images (16), separation of variables (18), and superposition (18,19) have been used to solve Laplace's equation for a number of systems. A review of analytic solutions has been presented by Fleck (20).

The Schwarz-Christoffel transformation (21-23), a type of conformal mapping, provides a powerful tool for the solution of Laplace's equation in systems with planar boundaries. The Schwarz-Christoffel transformation has been used to obtain the primary resistance of a number of cell geometries with application to electrochemical processes (24-27). This method was used by Moulton (28) to derive the current and potential distribution for two electrodes placed arbitrarily on the boundaries of a rectangle. Moulton's solution provides an asymptotic solution for compact tension specimens with a small notch size. Theoretical calibration curves for fracture specimens have also been obtained through application of conformal mapping for a number of simple specimen geometries, such as center and edge-cracked plates with various starter notch or crack configurations (9-11). These are reviewed by Halliday and Beevers (12). Application of the Schwarz-Christoffel transformation is generally limited, however, by the difficulty of generating solutions to the resulting integrals. Analytic solutions allow calculation of the primary current and potential distributions throughout the cell, but are possible for a limited number of system geometries. Numerical evaluation of these integrals allows calculation of both the primary current distribution along the electrodes and the cell resistance. Orazem (15) has applied this method to the compact tension specimen.

Method of Solution

The geometry of a compact tension specimen for measurement of crack-growth in response to fatigue is presented in Figure 1. The dimensions

are according to ASTM standards for specimen design and are included within the figure. These standards are modified for the study of crack growth in response to steady tension. The envelope of the starter notch is typically small and the angle β is generally $\pi/6$ (30°). This study will also make use of a large notch with angle β equal to $\pi/2$ (90°) to illustrate a region where the numerical results of Orazem (15) apply. Specimens with large notches have been used in stress-corrosion cracking experiments to allow the solution properties near the growing crack tip to be probed. Under the ASTM standards, the test block must be sufficiently thick that edge effects do not influence the propagation of the crack as a plane. This requirement is consistent with analysis of the electrical resistance of this system as being that of a two-dimensional specimen of the shape presented in Figure 1 and of thickness d.

Under the assumption that current inputs and voltage measurement probes are placed directly opposite each other, the plane of crack growth can be regarded to be a plane of symmetry. Thus the specimen will have twice the electrical resistance of the system presented in Figure 2a, where constant potential surfaces are designated by RS and PQ and all other boundaries are considered to be insulating. The pin holes (see Figure 1) were assumed to be filled by a close-fitting pin with the conductivity of the test specimen. The specimen is placed in a complex coordinate system such that the line OA lies on the real-z axis. The coordinate system of Figure 2a is transformed through an intermediate half-plane t (see Figure 2b) to a coordinate system (Figure 2c) in which Laplace's equation can be solved easily.

The primary current distribution along the electrodes and the cell resistance can be calculated through application of the Schwarz-Christoffel transformation. Complex coordinate systems are used, thus

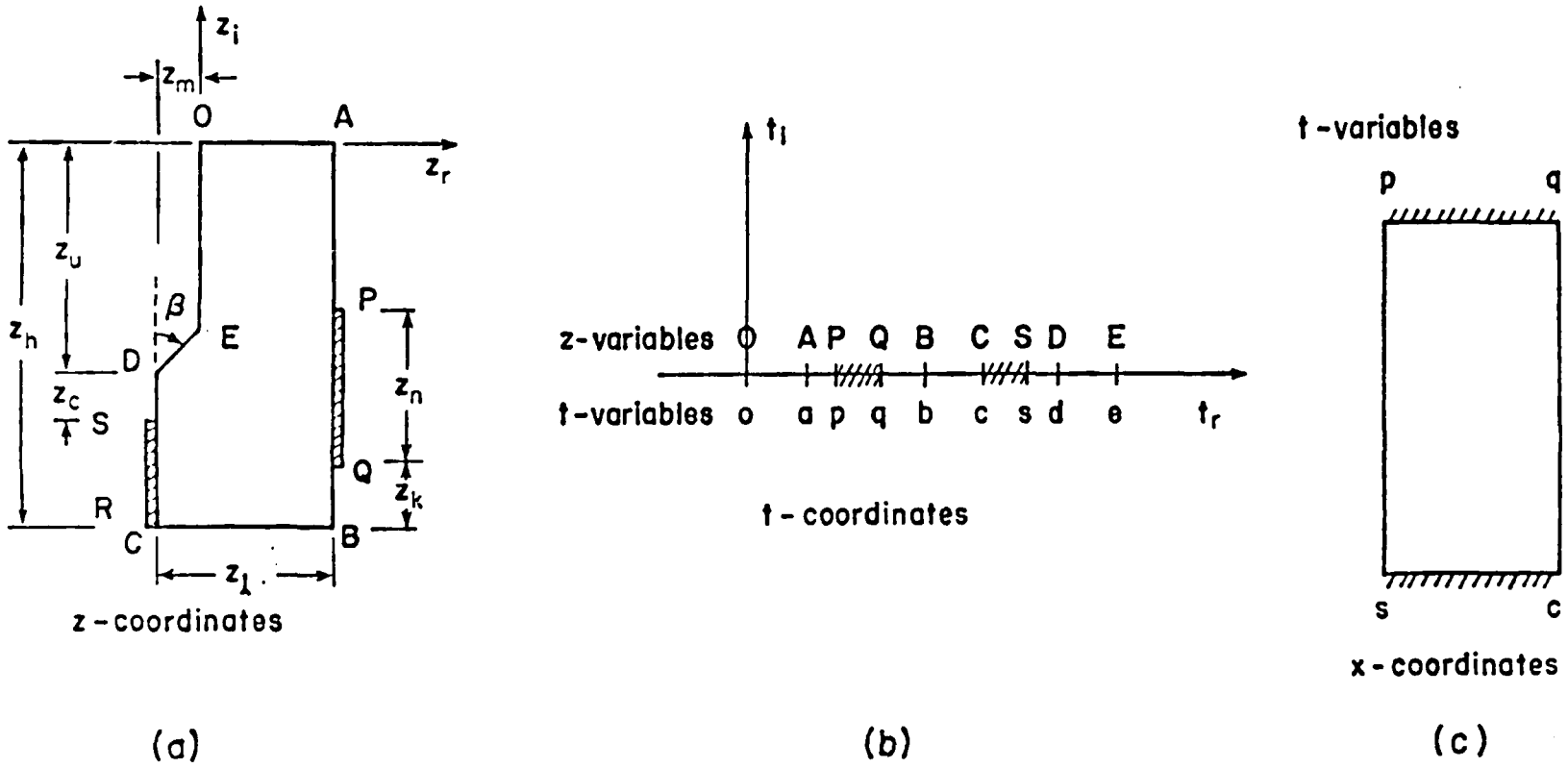

Figure 2. Schematic representation of a sectioned specimen and its transformation into coordinates:

(a) $z = z_r + j\, z_i$,

(b) $t = t_r + j\, t_i$, and

(c) $x = x_r + j\, x_i$.

$$z = z_r + jz_i .$$

The z-coordinate system is related to the t-coordinate system of Figure 2b by

$$z = \int_0^t \frac{(e-t)^{\beta/\pi}}{t^{\frac{1}{2}}(a-t)^{\frac{1}{2}}(b-t)^{\frac{1}{2}}(c-t)^{\frac{1}{2}}(d-t)^{\beta/\pi}}\, dt \ , \tag{4}$$

where a, b, c, d, and e are the values of t corresponding to z values of A, B, C, D, and E, respectively. The outside angle of D is represented by β such that $\beta/\pi = 1/2$ for a right angle corner. The electrodes PQ and CS correspond to pq and cs in the t-plane.

The variable χ (see Figure 2c) is related to the t-variables by the Schwarz-Christoffel transformation;

$$\chi = \int_0^t \frac{1}{(t-p)^{\frac{1}{2}}(q-t)^{\frac{1}{2}}(c-t)^{\frac{1}{2}}(s-t)^{\frac{1}{2}}}\, dt \ . \tag{5}$$

Solution of Laplace's equation for the χ-system yields the potential as a linear function of χ;

$$\Phi = \frac{\chi_i}{\chi_{i,max}} V \ , \tag{6}$$

where $\chi_{i,max}$ is the separation between electrodes cs and pq in the χ-system, and V is the potential difference between the electrodes. The potential drop in the original cell of Figure 1 is 2V. The current density is related to the potential derivative at the electrodes. The relationships among the potential derivatives at the electrodes in the χ, t, and z-coordinate systems are developed elsewhere. These relationships are the basis for a system of nonlinear integral equations that can be solved to obtain the current density along either electrode in the z-coordinate system. The dimensionless primary resistance $d\kappa R_i$ is obtained through integration over the electrode pq in the t-coordinate system:

$$d\kappa R = \frac{2x_{i,max}}{\int_p^q (t-p)^{-\frac{1}{2}}(q-t)^{-\frac{1}{2}}(c-t)^{-\frac{1}{2}}(s-t)^{-\frac{1}{2}}dt_r} \qquad (7)$$

The derivation of equation (7) and the numerical method used in this calculation are presented by Orazem (15). The dimensionless electrical resistance is a function of the angle β, three geometric ratios associated with cell shape (e.g., z_ℓ/z_h, z_m/z_h, and z_u/z_h), and three geometric ratios associated with electrode placement (e.g., z_k/z_h, z_n/z_h, and z_c/z_h). In the limit of the starter envelope area approaching zero, the electrical resistance approaches that of a rectangle with appropriately-placed electrodes. The solution for this problem has been presented by Moulton (28) in terms of tabulated elliptic functions (29).

The dimensionless resistance calculated in this way is that for the entire specimen. This resistance is related to that obtained from the measured potential drop $d\kappa R_1$ by

$$d\kappa R = d\kappa R_o + d\kappa R_1 \qquad (8)$$

where $d\kappa R_o$ is the dimensionless resistance obtained from the potential drop between the current inputs and the leads for potential drop measurement. The term $d\kappa R_o$ may be expected to be independent of crack length for specimens with a large notch size.

Results and Discussion

The theoretical results of Orazem (15) cannot be applied directly to the calibration of compact tension specimens for which the potential drop is measured at locations different than the current inputs. Aronson and Ritchie (14) state that the top surface close to the notch is the preferred location for positioning leads for measurement of potential differences across the

cracked region. This location minimizes errors associated with the uncertainty of probe location and with contact resistances associated with the current inputs. The resistance obtained as a function of crack length with leads separated from the current inputs can be related to the work of Orazem (15) under the assumption that the residual resistance is independent of crack length. This assumption is valid for specimens with a large notch area. Such specimens have been used to study stress corrosion cracking where the large notch allowed the introduction of probes near the crack tip. The analysis of this method is therefore presented in terms of the influence of notch size and the applicability of equation (3) as a calibration curve for specimens with a small notch size.

The Influence of Notch Size

The potential drop method was calibrated by optical measurement of the growing crack on the surface of a specimen subject to fatigue. The potential drop was measured between leads located at position V and between current inputs. The current was held at 50 Amps, and the magnitude of the potential drop measured across the notch ranged from 0.5 to 2 mV. The potential drop measured between current inputs ranged from 6 to 10 mV. The potential drop measured between current inputs had a significant amount of scatter due to the variation of the contact resistance with the tension applied to the specimen. These data were therefore discarded, and the analysis was based upon the potential drop measured between the potential leads as shown in Figures 1 and 3.

Calibration data are presented in Figure 4 for specimens with large rectangular notches (see Figure 3). These specimens were constructed by precracking the specimen with a narrow notch by fatigue and subsequently

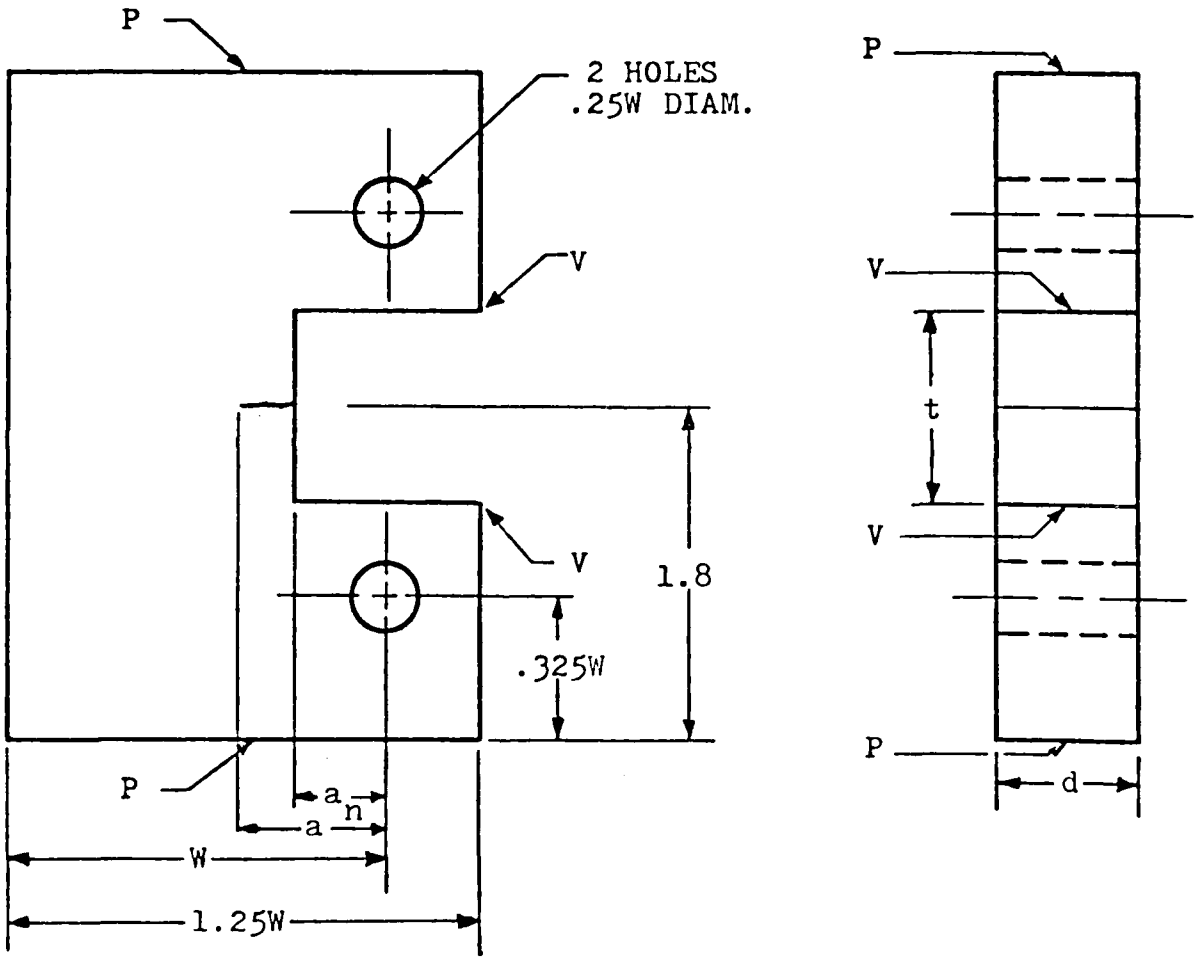

Figure 3. Schematic representation of a compact tension specimen with a large notch. The locations of current inputs are represented by P, and the location of voltage measurement leads are represented by V.

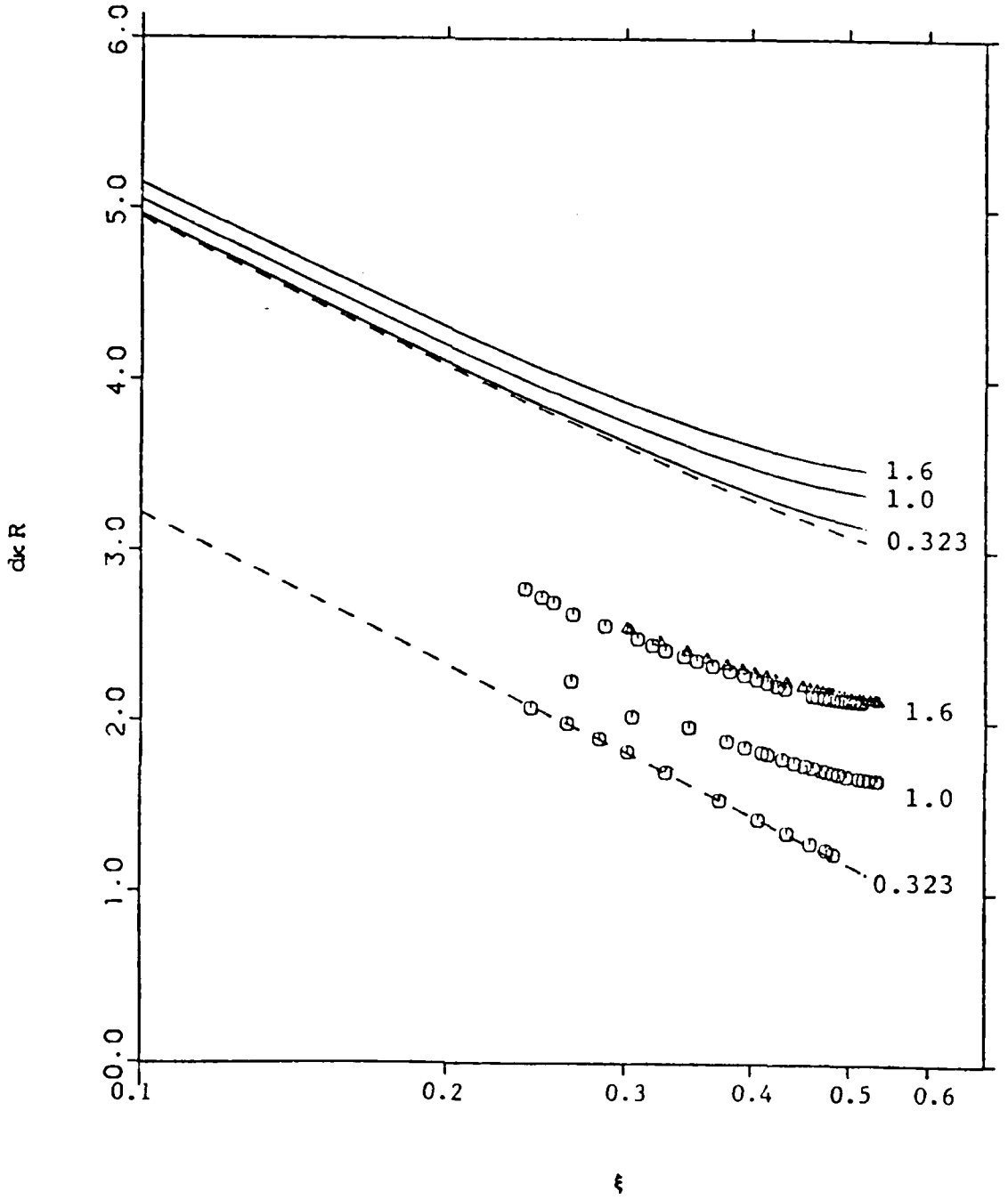

Figure 4. Dimensionless resistance of the specimen of Figure 3 as a function of the dimensionless crack length variable defined in equation (3a) with notch size as a parameter. Solid lines are the calculated values from equation (7), the upper dashed line is the calculated values obtained from Moulton's solution, and the lower dashed line is obtained from equation (3). All data are for a 7075-T6 aluminum alloy; the different symbols for the largest notch indicate repeated experiments.

machining the large notch. Data are presented for notch widths of 0.323, 1.0, and 1.6 inches. The results of numerical calculations for these geometries are presented as solid lines in Figure 4. The upper dashed line is the asymptotic solution given by Moulton (28). The calculated resistance is higher than that obtained from the experiments because the data represent the resistance between potential leads, whereas the calculations provide the resistance of the entire specimen. Under the assumption that the residual resistance is independent of crack length, the data can be adjusted according to equation (8). These adjusted data are presented in Figure 5. The assumption that dR_1 is independent of crack length is strictly valid for large notches, but fails for the smaller notch as shown in Figure 5. The results presented in Figure 5 provide experimental verification for the numerical results of Orazem (15) for large notch sizes and support his conclusion that small notches provide optimal sensitivity of the potential drop method to crack lengths.

The results for the specimen with the smaller notch indicate that the residual resistance is a function of crack size for small notches such that the asymptotic solution for long cracks is followed even for short cracks. This result is perhaps both surprising and fortuitous. The simple form of the asymptotic solution for long crack lengths, valid in a region where knowledge of the crack length is critical, also applies for small crack lengths under the conditions that the potential drop is measured close to the notch and that the notch is small. These are precisely the optimal specimen configurations suggested by Aronson and Ritchie (14) and by Orazem (15).

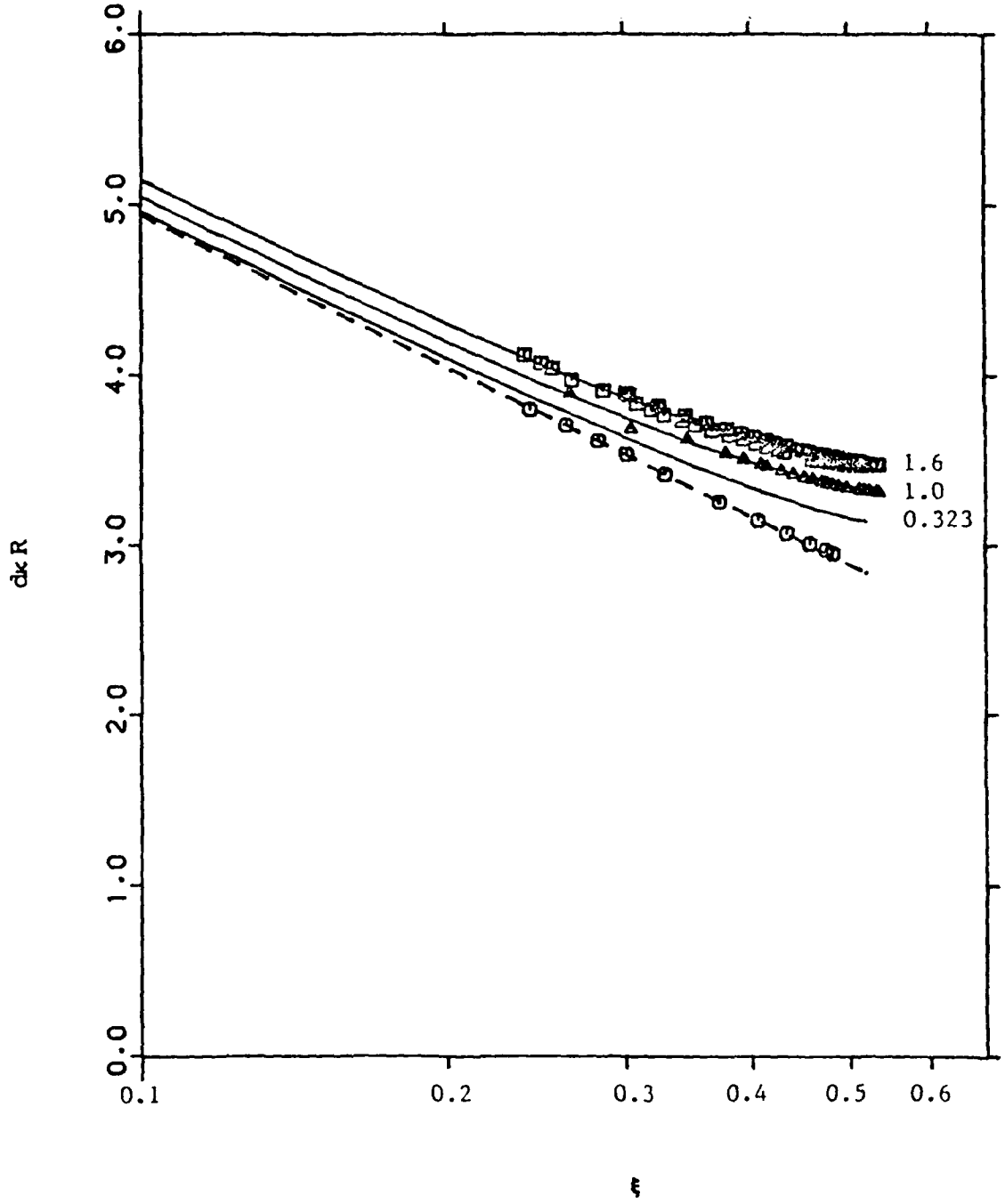

Figure 5. Dimensionless resistance of the specimen of Figure 3 as a function of the dimensionless crack length variable defined in equation (3) with notch size as a parameter. Solid lines are the calculated values from equation (7), and the dashed line is the asymptotic solution for long crack lengths. All data are for a 7075-T6 aluminum alloy; notch sizes are ○ 0.323 inches, Δ 1.0 inches, and □ 1.6 inches, respectively.

Calibration Procedure

Experimental calibration data are presented in Figure 6 for three specimens of experimental aluminum-lithium-magnesium alloys with small notches as shown in Figure 1. These alloys were obtained by a mechanical alloying process, and they differ only in carbon content. The solid line is the calculated value for this geometry which follows exactly Moulton's solution (28). The data most closely follow the asymptotic solution for long crack lengths. The relationship between these data and the traditional method for analysis of calibration data as described in the introductory section is seen in Figure 7. The dashed curve is the best fit according to equation (2). Equation (3) was used in this analysis as a two parameter model from which the electrical resistivity for the specimens was obtained. The resistivity was found to be 15.9 μΩ•cm for the specimen denoted by triangles, 17.4 μΩ•cm for the specimen denoted by squares, and 15.5 μΩ•cm for the specimen denoted by circles. The solid line follows equation (3) where the constant C_1 was equal to 0.097, 0.029, and 0.019, respectively. Independently measured values of the resistivity for these specimens were 14.2, 14.2, and 14.0 μΩ•cm, respectively. The first two values are for the same alloy; the deviation between resistivities obtained through the calibration data and the independent measurements can be attributed to uneven growth of the crack front. Deviation was most pronounced for samples which showed extensive curvature of the crack fronts. The extent of curvature was observed by examining the overload markings on the fracture surface. The specimen used for the large notch studies was a 7075-T6 aluminum alloy. The electrical resistivity obtained from the calibration data for this material was 6.41 μΩ•cm, and the independently measured value for this specimen was 5.9 μΩ•cm. The scatter of data for the calibration of large-notch specimens was smaller;

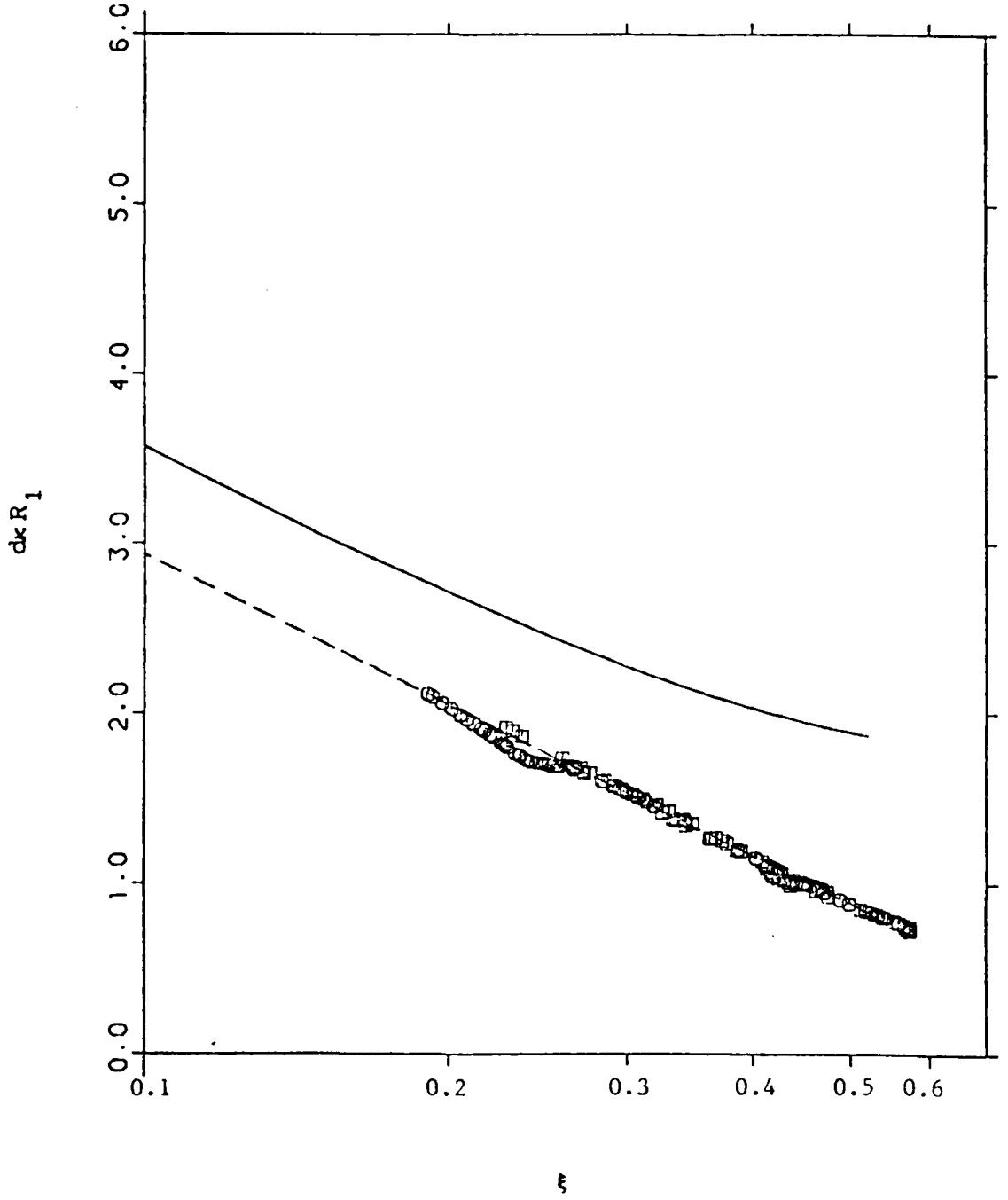

Figure 6. Dimensionless resistance of the specimen of Figure 1 as a function of the dimensionless crack length variable defined in equation (3). The solid line is the calculated values from equation (7), and the dashed line is obtained from equation (3). □ and Δ, repeated experiments for an Al-2.5Li-2.0Mg-1.1C-0.60 alloy; and , an Al-2.5Li-2.0Mg-0.7C-0.60 alloy.

however, equation (3), from which the resistivity was determined, could only be used for the specimen with a smaller notch. This is apparent in the presentation in Figure 8 of calibration data for specimens with a large notch.

These results show the power of this approach in analyzing calibration data. As a two parameter model, the calibration data can provide a value for the electrical resistivity of the specimen. This may prove to be especially useful for experimental alloys for which literature values are not available. The shape of the calibration curve is based upon fundamental principles, and the additive constant merely shifts the curve up or down. This is evident in the analysis of the data for large notch specimens as shown in Figure 8. The model curves shown as solid lines in Figure 8 differ only in the value for the additive constant. Through this analysis, coupling of the electrical resistance method with other techniques for monitoring crack length will allow evaluation of such anomalies as uneven crack growth, crack closure, and changes in the electrical conductivity near the growing crack tip. Such an anomaly is seen in the data presented in Figure 7.

Conclusion

Equation (3) provides a useful tool for the calibration of the potential drop method for measuring crack lengths in compact tension specimens of the usual dimension. This equation follows the correct asymptotic solution for long crack lengths and holds for even very short crack lengths for specimens with a small notch. For this reason, equation (3) can be used to evaluate the calibration data for anomalies such as those associated with uneven crack growth, crack closure, and changes in conductivity near the crack tip. Equation (3) can also be used as a two parameter model from which the electrical resistivity of the specimen can be determined. The data presented here for specimens with large notches support the results of Orazem (15)

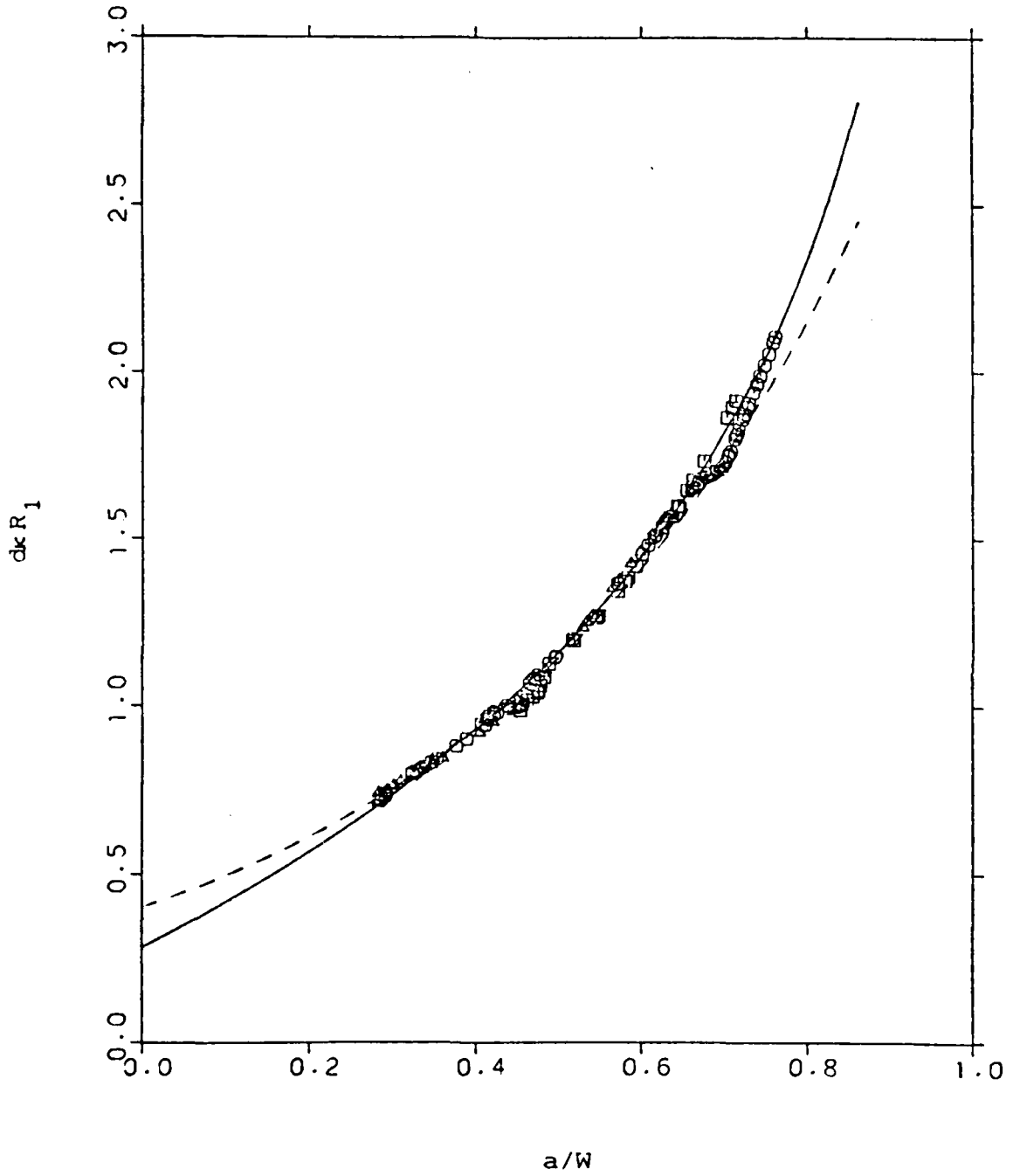

Figure 7. Dimensionless resistance of the specimen of Figure 1 as a function of a/W. Solid lines are calculated values from equation (3), and the different symbols indicated repeated experiments.

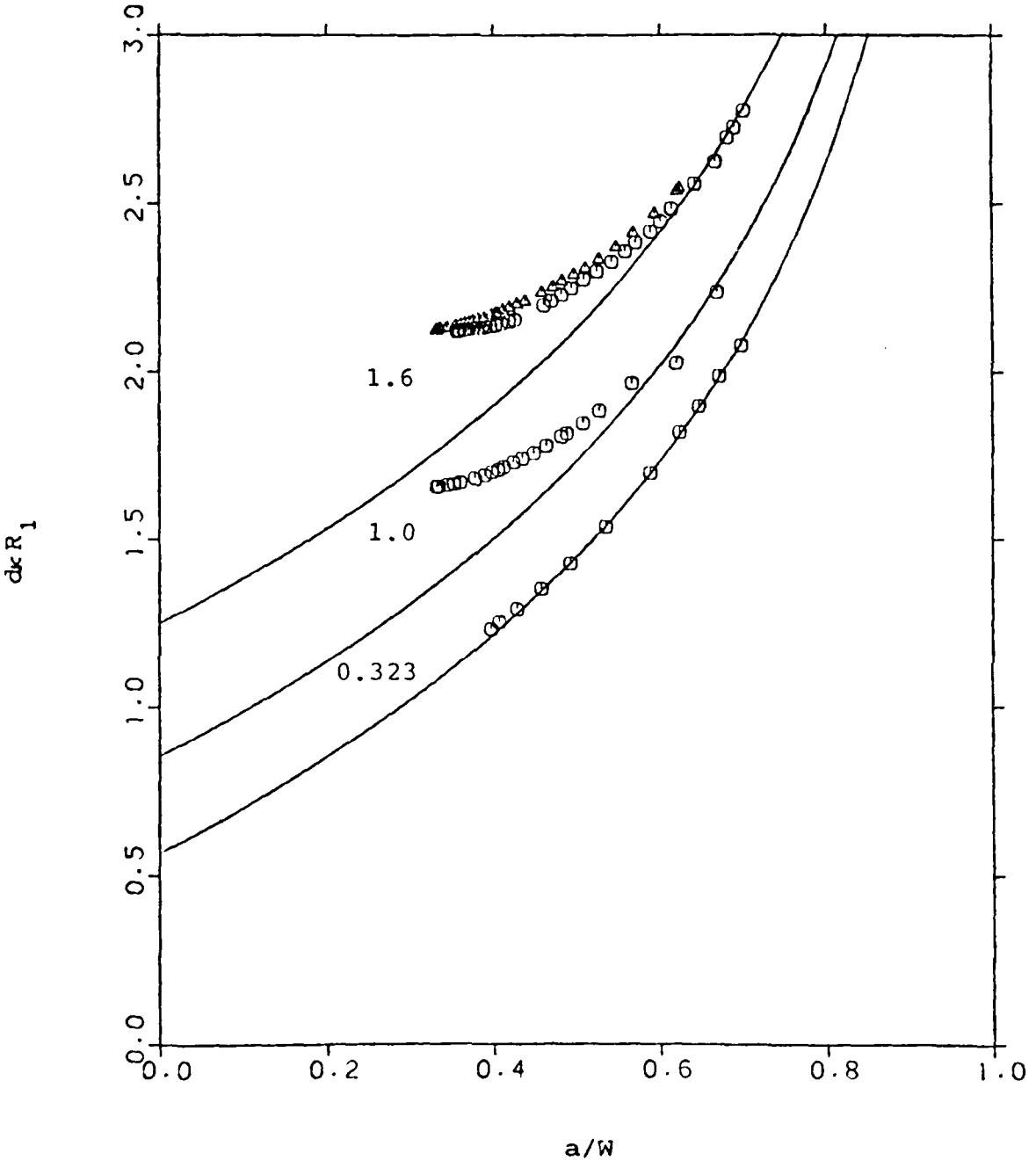

Figure 8. Dimensionless resistance of the specimen of Figure 3 as a function of a/W with notch width as a parameter. Solid lines are the calculated values from equation (3), and the different symbols for the largest notch indicate repeated experiments.

obtained by a numerical method coupled with conformal mapping, and support the conclusion (14,15) that the optimal specimen geometry includes potential measurement at the top of the specimen across a small notch.

Acknowledgements

This material is based on work supported in part by the Air Force Office of Scientific Research, United States Air Force Systems Command, Grant No. AFOSR-83-0061, Dr. Alan Rosenstein, program manager (W. Ruch) and by the Center for Innovative Technology , Grant No. CIT-MAT-85-027 (M. E. Orazem)

NOTATION

Roman Characters

a	crack lengthm em (see Figure 1)
C_k	adjustable parameters for equations (1), (2), or (3)
d	specimen thickness, cm (see Figure 1)
h	distance defined in Figure 1, cm
i	current density, mA/cm^2
j	$\sqrt{-1}$
R	half-cell resistance, ohms
V	potential drop, V
V_a	potential drop measured for crack length a, V
V_{ao}	potential drop measured for a reference crack length ao, V
W	distance defined in Figure 1, cm
z_c	crack length, cm (see Figure 2a)
z_h	cell height, cm (see Figure 2a)
z_k	height of electrode for resistance measurement, cm (see Figure 2)
z_ℓ	length of half-cell, cm (see Figure 2a)
z_m	half-width of starter-crack notch, cm (see Figure 2a)
z_n	width of electrode for resistance measurement, cm (see Figure 2a)
z_u	depth of starter-crack notch, cm (see Figure 2a)

Greek Characters

α	angle at corner of electrode and insulating wall
β	angle of notch (see point D in Figure 2a)
κ	conductivity, mho/cm
ξ	dimensionless length of uncracked ligament (see equation 3a)
ρ	resistivity, $\mu\Omega \cdot cm$
Φ	electrical potential, V

Subscripts

i	imaginary
r	real

REFERENCES

1. "Standard Test Method for Plane-Strain Fracture Toughness of Metallic Materials," in Annual Book of ASTM Standards, Part 10, American Society for Testing and Materials, Philadelphia, PA, 1979, 540-561.

2. Barnett, W. J., and A. R. Troiano, "Crack Propagation in the Hydrogen-Induced Brittle Fracture of Steel," Journal of Metals, 9 (1957), 486-494.

3. Tchorzewski, R. M. and W. B. Hutchinson, "Anisotropy of Fracture Toughness in Textured Titanium-6Al-4V Alloy," Metallurgical Transactions, 9A (1978), 1113-1124.

4. Stubbington, C. A. and S. Pearson, "Effect of Dwell on the Growth of Fatigue Cracks in Ti-6Al-4V Alloy Bar," Engineering Fracture Mechanics, 10 (1978), 723-756.

5. Beevers, C. J., R. J. Cooke, J. F. Knott, and R. O. Ritchie, "Some Considerations of the Influence of Subcritical Cleavage Growth During Fatigue Crack Propagation in Steels," Metal Science, 9 (1975), 119-126.

6. Blades, N. A. J., W. J. Plumbridge, and D. Sidey, "High Temperature Fatigue Crack Propagation in Aluminum Alloy RR58," Materials Science and Engineering, 26 (1976), 195-207.

7. Johnson, H. H. and A. M. Willner, "Moisture and Stable Crack Growth in a High Strength Steel," Applied Materials Research, 4 (1965), 35-40.

8. Hackett, E. M., J. R. Scully, and P. J. Moran, "Influence of Cathodic Polarization on the Fracture Properties of High Strength Steels in Seawater," presented at the Meeting of the Electrochemical Society, Washington, D.C., October 13, 1983.

9. Carlsson, A. J., "Experimental Studies of Fracture Propagation," Transactions of the Royal Institute of Technology, Stockholm, Sweden, 189 (1962), 1-55.

10. Johnson, H. H., "Calibrating the Electrical Potential Method for Studying Slow Crack Growth," Materials Research and Standards, 9 (1965), 442-445.

11. Clark, G. and J. F. Knott, "Measurement of Fatigue Cracks in Notched Specimens by Means of Theoretical Electrical Potential Calculations," Journal of Mechanics and Physics of Solids, 23 (1975), 265-276.

12. Halliday, M. D. and C. J. Beevers, "The D. C. Electrical Potential Method for Crack Length Measurement," in The Measurement of Crack Length and Shape During Fracture and Fatigue, C. J. Beevers, editor, Chameleon Press, Ltd., London, United Kingdom.

13. Ritchie, R. O. and K. J. Bathe, "On the Calibration of the Electrical Potential Technique for Monitoring Crack Growth Using Finite Element Methods," International Journal of Fracture, 15 (1979), 47-55.

14. Aronson, G. H. and R. O. Ritchie, "Optimization of the Electrical Potential Technique for Crack Growth Monitoring in Compact Test Pieces Using Finite Element Analysis," Journal of Testing and Evaluation, 7 (1979), 208-215.

15. Orazem, Mark E., "Calculation of the Electrical Resistance of a Compact Tension Specimen for Crack-Propagation Measurements," Journal of the Electrochemical Society, 132 (1985), 2071-2076.

16. Kasper, Charles, "The Theory of the Potential and the Technical Practice of Electrodeposition," Transactions of the Electrochemical Society, 77 (1940), 353-384; 78 (1940), 131-160; 82 (1942), 153-184.

17. Newman, John, "Resistance for Flow of Current to a Disk," Journal of the Electrochemical Society, 113 (1966), 501-502.

18. Miksis, J. J., Jr., and J. Newman, "Primary Resistance for Ring-Disk Electrodes," Journal of the Electrochemical Society, 123 (1976), 1030-1036.

19. Pierini, P., and J. Newman, "Potential Distribution for Disk Electrodes in Axisymmetric Cylindrical Cells," Journal of the Electrochemical Society, 126 (1979), 1348-1353.

20. Fleck, R. N., Numerical Evaluation of Current Distribution in Electrochemical Systems, M. S. Thesis, University of California, Berkeley, September 1964 (UCRL-11612).

21. Churchill, R. V., Complex Variables and Applications, second edition, McGraw-Hill Book Company, New York, 1960.

22. Copson, E. T., An Introduction to the Theory of Functions of a Complex Variable, Oxford University Press, London, 1935.

23. Bowman, F., Introduction to Elliptic Functions with Applications, John Wiley and Sons, New York, 1953.

24. Hine, F., S. Yoshizawa, and S. Okada, "Effect of the Walls of Electrolytic Cells on Current Distribution," Journal of the Electrochemical Society, 103 (1956), 186-193.

25. Wagner, C., "Calculation of the Current Distribution at Electrodes Involving Slots," Plating, 48 (1961), 997-1002.

26. Newman, J., "The Fundamental Principles of Current Distribution in Electrochemical Cells," in Electroanalytical Chemistry, (A. J. Bard, editor), 6 (1973), 187-352.

27. Orazem, M. E. and J. Newman, "Primary Current Distribution and Resistance of a Slotted-Electrode Cell," Journal of the Electrochemical Society, 131 (1984), 2857-2861.

28. Moulton, H. F., "Current Flow in Rectangular Conductors," Proceedings of the London Mathematical Society (Ser. 2), 3 (1905), 104-110.

29. Milne-Thomson, L. M., "Jacobian Elliptic Functions and Theta Functions," and "Elliptic Integrals," Chapters 16 and 17 in the Handbook of Mathematical Functions, edited by M. Abromowitz and I. A. Stegun, Dover Publications, New York, 1972.

TASK II. FATIGUE CRACK GROWTH AND FRACTURE TOUGHNESS BEHAVIOR OF AN Al-Li-Cu ALLOY

K. V. Jata and E. A. Starke, Jr.

Slip behavior, fracture toughness and fatigue thresholds of a high purity Al-Li-Cu alloy with Zr as a dispersoid forming element have been studied as a function of aging time. The fracture toughness variation with aging time, has been related to the changes in slip planarity, i.e. slip band spacing and width. Although the current alloy exhibits planar slip for all aging conditions examined, the crack initiation toughness, K_{1c}, compares favorably with those of 2xxx and 7xxx aluminum alloys. Near threshold fatigue crack growth results in air and vacuum suggest that, irregularities in the crack profile and the fracture surfaces and slip reversibility are some of the major contributing factors to the crack growth resistance of this alloy.

Introduction

Aircraft designers are constantly striving to achieve minimum weight in order to cut fuel consumption and improve overall performance. Reducing the density of structural materials has been shown to be the most efficient solution to this problem (1). Since aluminum alloys make up between seventy and eighty percent of the current aircraft weight, recent alloy development programs have focused on reducing the density of these materials (2). Lithium additions to aluminum provide the greatest reduction in density of any alloying element and offer the additional advantage of increasing the elastic modulus. However, Al-Li-X alloys often exhibit low ductility and fracture toughness.

Various modifications in alloy chemistry and fabricating techniques have been used in an attempt to improve the ductility while maintaining a high strength. Copper, Mg and Zr solute additions have been shown to have beneficial effects (3). Magnesium and Cu improve the strength of Al-Li alloys

through solid solution and precipitate strengthening, and can minimize the formation of precipitate free zones (PFZ) near grain boundaries. Zirconium, which forms the cubic Al_3Zr coherent dispersoid, stabilizes the subgrain structure and suppresses recrystallization.

The goals of most Al-Li-X alloy development programs include improvements in density and modulus with equivalent or improved damage tolerance and corrosion properties compared with currently used materials, e.g. 7075 and 2024 (4). Although there have been numerous reports on the relationship between composition, microstructure and monotonic properties of Al-Li-X alloys (5,6), there have been few studies on the cyclic properties and fracture toughness of these materials. This paper describes the fatigue crack propagation and fracture toughness of a new alloy based on the Al-Li-Cu system which is somewhat related to the Al-Li-Cu alloy 2020 that was commercially available in the 1960's.

Experimental Procedures

The actual chemical composition of the Al-Li-Cu alloy used for the present investigations is shown in Table 1. It is similar in composition to the Al-Li-Cu alloy, M2, recently studied by Feng et al.(7), except for slightly lower Cu and Cd and slightly higher Li contents. In addition to the above, low levels of Fe and Si were maintained to minimize the amount of constituent phases. Zirconium was added as the dispersoid forming element.

The material was obtained from Reynolds Metals Company in the form of 27.7 mm thick plates. The original cast ingots were homogenized in an argon atmosphere as follows: (i) Heated at 523 K/hour to 673 K, held 48 hours, (ii) heated at 298 K/hour to 763 K, held 18 hours, (iii) heated at 298 K/hour to 788 K held for 30 minutes and fan cooled. The ingots were scalped on the surface to 69.8 mm thick and then cleaned. The hot rolling was performed in

three steps, preheated to 733 K, held for one hour, hot rolled from 69.8 mm to 57.1 mm, reheated to 733 K, hot rolled to 44.5 mm, reheated to 671 K and hot rolled to a final thickness to 27.7 mm.

The alloy was solutionized in a salt bath at 78 K for 30 minutes, quenched in ice water, stretched 2 percent and aged in an oil bath at 433 K for different periods of time, Table 2. Fracture toughness was measured on 11 mm thick compact tension samples in the L-T orientation and a conditional K_{1c} value for fracture toughness was obtained from the load-crack opening displacement plots by choosing the 5 percent secant offset line. Of all the samples tested only the two underaged samples did not meet the ASTM thickness criterion $b \geq 2.5\ (K_{1c}/\sigma_{ys})^2$. A thickness of 54 mm would have been required for the underaged samples for a valid K_{1c} test.

Crack propagation tests were conducted on compact tension specimens in laboratory air (R.H. ~ 45 percent) and a vacuum of 10^{-5} torr at 295 K using a R ratio of 0.1 and a frequency of 30 Hz. The crack propagated in the long transverse direction on a plane normal to the rolling direction. Crack growth was monitored with a travelling microscope and load versus crack opening displacement curves were generated by the elastic compliance techniques. Near threshold crack growth rates were obtained by the load-shedding scheme. At every load level the crack was allowed to propagate the distance equal to at least three times the cyclic plastic zone size and then the load was decreased by less than three percent.

The microstructures were examined by optical, scanning and transmission electron microscopy. Thin foils for transmission work were obtained with a dual jet Tenupol apparatus by using fifty percent nitric acid-methanol mixture at 253 K and a potential difference of 15 volts. Fracture surfaces were examined with a scanning electron microscope.

Results and Discussion

A. Microstructure and Tensile Properties

Optical metallography revealed a predominately unrecrystallized grain structure. However, some recrystallization occurred during solution treatment as shown in the micrograph of the L-S section, Figure 1a. A high degree of recrystallization has been shown to be undesirable in Al-Li-X alloys since secondary crack paths are invariably associated with recrystallized grains (8). Thus from a ductility point of view, it is advantageous to select a low solutionization temperature in order to suppress recrystallization (8). However, if the temperature is too low, some strength is lost due to incomplete solutionizing prior to aging. In the present work a solution treatment temperature of 788 K was found to be an optimum temperature to achieve the desired strength level, while minimizing the degree of recrystallization. No coarse precipitate, which would be associated with an incomplete solution heat treatment were observed. Figure 1a.

A detailed TEM examination was performed to study the microstructure of the alloy. Bright field images revealed the subgrains in the unrecrystallized structure to be approximately 5 microns in diameter, Figure 1b. Precipitate characterization was performed using an exact [100] zone to detect Al_3Li and Al_2Cu precipitates, and an exact [110] zone to detect Al_2CuLi precipitates (9,10,11). The Al_3Li (δ') could not be imaged as individual precipitates in any aging condition using the Al_3Li-Al_3Zr superlattice spot shown in Figure 2a. However, the "donut" contrast of the spherical precipitates shown in Figure 2b may indicate a ternary Al-Zr-Li phase (12). Since it was impossible to isolate the Al_3Li-Al_3Zr superlattice spots from the streaking associated with the θ' (Al_2Cu) phase, θ' is also observed in Figure 2b. The θ'

precipitates appeared as plates in two orthogonal directions and as a plate with a line of no-contrast as the third variant, Figure 2b, consistent with previous observations (13).

Many of the 0' precipitates in one of the variants appear to be more eliptical than normally observed in Al-Cu binary alloys (14). This may indicate that Al_3Li has nucleated on one of the three variants of the Al_2Cu precipitates. It may also be due to the incorporation of some Li in the 0" phase. Silcock (15) has theorized that $Al_{7.5}Cu_4Li$ (T_B) forms continuously from 0' by the replacement of Al atoms by Li, and Noble et al. (16) have shown that Li may cluster with Cu to form plate-shaped zones having a (100) habit plane similar to 0'. Nobel and Thompson (10) also observed that δ' coprecipitated with 0' and Al_2CuLi (T_1) in an Al-3.5Cu-1.5Li alloy during the aging at 150 C. No T_1 precipitates were observed for either the UA1 or UA2 conditions, but both 0' and T_1 were present in the PA condition, Figure 2c in our study.

During artificial aging 0' coarsens and transforms to the equilibrium 0 phase which is incoherent with the matrix. The formation of the 0 phase is normally accompanied by softening in Al-Cu binary alloys. However, for all of the aging conditions used in this study streaks associated with 0' were present and no 0 diffraction spots were observed in the electron diffraction patterns. Streaks associated with 0' were still present even after 40 hrs at 160 C, Figure 3a, and DF electron micrographs using these streaks revealed the fine, coherent 0' precipitates, Figure 3b. This result is consistent with the results of Noble and Thompson (10) who showed that streaks associated with 0' were still present in an alloy of similar composition even after aging for one week at 190 C. After aging for 40 hrs at 160 C, diffraction patterns from the [110] zone contained streaks associated with T_1, Figure 3C, and DF electron

micrographs using these streaks revealed thin coherent T_1 precipitates, Figure 3d. The coherency of T_1 was verified by the absence of misfit dislocations using bright field images employing different g vectors in two-beam conditions, Figure 4. Our analysis, along with the results of others (9-11,14,17) suggest that both θ' and T_1 remain coherent across their habit planes for all of the aging treatments used in this study.

The tensile properties obtained at various aging times are listed in Table 2. The peak strength was found to be lower than that of the M2-T651 alloy investigated by Feng et al. (7). This is attributed to the lower Cu content in the present alloy and thus a lower volume fraction of the major strengthening precipitates, θ' and T_1. The slip behavior was studied by TEM analysis of thin foils obtained from regions adjacent to the fracture surface of the tensile samples. Slip bands in {110} type slip planes were chosen and the imaging of the bands was performed using a g = 220 or 220. Four to five different grains were chosen in each aging condition and average values of the slip band width and spacing was obtained. Representative micrographs of the slip character obtained with a [110] zone axis show planar slip behavior observed for all the aging conditions employed, Figure 5 (a-d). In the as-quenched condition only a few planar slip bands were observed at near fracture strain and only in certain grains as most of the deformation was homogeneously distributed. These slip bands may be associated with some $Al_3Li(\delta')$ (although not observed) or short-range order (18,19) being present in the as-quenched condition. It is observed that with progressive aging the fine relatively homogeneous slip changes to well defined intense slip bands in the peakaged condition. These bands become more prominent, the separation between them increases, and their width decreases as aging progresses as shown in Figures 6 and 7. It should be noted that the volume fraction of T_1

increase with aging up to the peakaged condition. The slip bands still persist in the slightly overaged condition, Figure 5d, due to the presence of semicoherent precipitates. However, they are more diffused when compared to the peakaged condition suggesting a slight reversal to relatively homogeneous slip. The slip bands are most often continuous across the subgrains.

The changes in the monotonic properties and slip behavior with aging show that the increase in yield strength is accompanied by increasing amounts of strain localization in the slip bands and a concomitant decrease in the strain hardening exponent and ductility level. The formation of sharp slip bands is a consequence of dislocations shearing the precipitates. When shearing occurs the strengthening effect of the precipitates is reduced, the slip plane weakens, and slip occurs preferentially on these planes (20-22). This results in an inhomogeneous slip distribution which almost always leads to a considerable loss in ductility and macroscopically brittle fracture as particle hardening is increased (23-26). The tendency for inhomogeneous slip increases drastically with aging time until the deformation mode changes from dislocation shearing to dislocation looping, at which time the homogeneity of deformation increases. This is easily understood when considering the strengthening associated with shearable particles.

Using, as an example, the model developed by Gleiter and Hornbogen (20,21) for misfit-free, ordered particles (such as Al_3Li) the increase in the critical resolved shear stress, $\Delta\tau_o$, associated with the strengthening precipitates is given by:

$$\Delta\tau_o = 0.28\, G^{-1/2} b^{-2}\, \gamma^{3/2} f^{1/2} r_o^{1/2} \qquad (1)$$

where γ is the antiphase boundary energy, G is the shear modulus, b the Burgers vector, f the volume fraction of precipitates, and r their radius. We

note that the strength increases with both particle size and volume fraction. Although the particular strengthening mechanism, i.e. coherency hardening, surface hardening, chemical or order hardening, stacking fault hardening, and modulus hardening, may vary among different alloy systems, the strengthening associated with shearable particles always increases with both volume fraction and particle size, (27) similar to the expression developed by Gleiter and Hornbogen. Consequently the degree of work softening possible during deformation and thus the tendency towards localized slip is proportional to the magnitude of $r^{\frac{1}{2}}f^{\frac{1}{3}}$ (19,24). If one examines the local change in critical resolved shear stress per number of passing dislocations, one observes that the rate of change increases as the volume fraction increases and the particle size decreases (28). However, for very small particles the absolute change in shear stress is small so the degree of strain localization is also small.

When the yield strength is exceeded in an age hardened alloy local softening, equal in magnitude to that associated with the hardening of the shearable precipitates, occurs since the particles are destroyed by the slip dislocations. The dislocations form intense slip bands which impinge upon the grain boundaries. The slip bands are usually not confined to a single slip plane but cover a small volume in which the spacing of the individual active slip planes may be of the order of the atomic spacing (24). When the local work softening within the slip band is complete, the slip band strain-hardens internally until the stress of the surrounding aged matrix is reached (26) or fracture occurs. Consequently, in microstructures with different degrees of age hardening the slip bands contain different numbers of dislocations, with the local dislocation density increasing with increasing degree of age hardening, i.e. with $f^{\frac{1}{3}}r^{\frac{1}{2}}$.

The lower degree of strain localization associated with the underaged conditions results in a larger capacity for strain accumulation. This is reflected both by the high strain hardening exponents and strains to fracture. With aging the strain hardening exponent decreases, reaching a minimum in the peakaged condition, due to increased work softening in the slip bands (27). Since the majority of the deformation is localized, the net effect is a lower ductility level. Beyond the peakaged condition one would expect slip to become more homogeneous since overaging is normally accompanied by a change in deformation mechanism from dislocations shearing particles to dislocations looping and bypassing particles. In actuality for most aluminum alloys this transition in deformation mode normally begins before the peak strength is reached as some of the larger strengthening precipitates become incoherent and cannot be sheared. Consequently, for most age hardening aluminum alloys the highest degree of strain localization is observed for a slightly underaged condition. However, θ' and T_1 phases were observed to maintain their coherency in the peakaged condition for the thermal treatments used in this study and the transition in deformation mode only occurs after overaging. An increase in strain hardening exponent should accompany this change in deformation mode, and this was observed in the present study. However, an increase in strain-to-fracture is not observed in OA-2 and OA-3, Table 2, because the equilibrium precipitates that form at grain boundaries during overaging, and the associated precipitate-free-zones, aid the void nucleation and coalesence. Transmission electron micrographs of OA-2, Figure 5d, showed that planar slip persisted in the overaged condition, although the deformation was more homogeneous than that observed for the PA condition. This is not surprising since both θ' and T_1 were observed to maintain coherent interfaces with the matrix across their habit planes, for all aging conditions studied,

and may continue to be sheared even though the drop in yield strength for OA-1,2, and 3 indicated that some particles should be bypassed by dislocations. An alternative explanation for the drop in yield strength is that there is a decrease in the volume fraction of strengthening precipitates associated with the precipitation of the equilibrium phases at grain boundaries in the late stages of aging. The shearing of T_1 was observed in DF TEM's of an OA-2 tensile sample that had been give 2% plastic strain, Figure 8a. An example of dislocation bypassing in this microstructure is also shown in Figure 8b.

The effect of slip localization on the tensile fracture can be observed in the fractographs, Figure 9 for an underaged and overaged alloy. In both cases transgranular shear fracture is observed along with some voids associated with precipitate particles and/or slip band intersections. There was little evidence of intersubgranular fracture although secondary cracking was observed along the high angle grain boundaries of the overaged sample, Figure 9b. This intense secondary cracking may be associated with the small recrystallized grains observed in Figure 1a, but is most likely due to the presence of coarse equilibrium precipitates at the high angle grain boundaries and the presence of a PFZ adjacent to the boundary. The decrease in ductility with aging seems to be simply due to the extensive shear localization and accompanying slip band softening up to the peakaged condition. Beyond the peakaged condition larger equilibrium precipitates on the grain boundaries give rise to intergranular cracking which further reduces the ductility.

B. Near Threshold Fatigue Crack Propagation

The results obtained from the fatigue crack growth tests in air (R.H. 45 percent) and in vacuum ($<10^{-5}$ torr) are shown in Figures 10(a) and (b) as plots of crack propagation rates da/dN versus the stress intensity factor

range ΔK. The near threshold fatigue crack growth rates increased and the threshold stress intensities (Table 3) decreased with aging in both air and vacuum. Furthermore, there is an enhancement of the fatigue crack growth resistance in vacuum for similar aging conditions. The crack closure data obtained from the compliance versus load curves has been expressed (29) in the form of the closure stress intensity factor $\Delta K_{th}^{Cl} = K_{th}^{Cl} - K_{th}^{min}$, and the intrinsic (or effective) stress intensity factor $\Delta K_{th}^{i} = \Delta K_{th}^{obs} - \Delta K_{th}^{Cl}$, as shown in Table 3. These values indicate that the intrinsic fatigue crack growth thresholds follow the same trend as the apparent or observed values, for the aging conditions tested here.

Figure 11 shows the crack paths for the alloy tested in air in the under and overaged conditions. The observed deflections appear to be due to the crack propagating along the slip bands. It is not surprising that extensive crack deflections also occurred in the overaged alloy since slip planarity is maintained and intense slip bands are available for crack propagation paths. Suresh and Vasudevan have also observed (30) equal degrees of crack deflections in under and overaged conditions in low Li containing alloys.

The fracture surface features shown in Figure 12, reveal that the mode of crack growth is highly crystallographic in the low crack growth rate region. Extensive faceting was observed in vacuum and the fracture surfaces were considerably rougher than those observed on the samples tested in air. The lower crack path tortuosity in air as compared to that in vacuum could be due to the aggressive air environment reducing the amount of irreversible plasticity needed for the crack to propagate (31). There is the possibility for oxide formation which might be expected to enhance closure and thus giving an apparent higher threshold. However, Vasudevan et.al. (32) showed by SIMS

that the thickness of the oxide for a similar alloy 2020 is considerably smaller than the crack opening displacement, suggesting that the oxide contribution, if any, would be negligible.

Figure 13 compares the results obtained for the Al-Cu-Li alloy with those of a thermomechanically processed 7475 (33). The fatigue crack growth rates and thresholds of the Al-Cu-Li alloy are better than those of the 80 μm grain size 7475. Several investigators have proposed that the fatigue crack growth rates decrease with increasing modulus (34), thus indirectly predicting that Li-containing Al alloys would have improved FCP resistance. Therefore, a more realistic comparison of the two materials may be obtained by normalizing the stress intensity range with Youngs' modulus since the yield stresses are approximately the same. As shown in the normalized curves of Figure 13(b), the fatigue growth rate curves remain below the 7475 alloy suggesting that the improvement is not due to the modulus effect alone. In a similar comparison, Vasudevan et al. (32) came to the conclusion that the crack deflections in the 2020 alloy were a major cause for improved crack growth resistance over that of a 7075 alloy. A comparison of the crack deflections observed in 7475 (33) with those observed here also show that this mechanism may account for the improved crack growth resistance observed, although differences in slip reversibility may also be a contributing factor.

In the present alloy the crack propagation rates are higher in the overaged condition as compared to the peak and underaged conditions. These observations are consistent with earlier observations made by other investigators in age hardened systems (33,35,36). In these alloys, the dislocations shear the coherent precipitates and thus promote inhomogeneous slip in the under and peakaged conditions. In the overaged alloys, the coherency between the precipitates and matrix is reduced (although not lost) resulting in less

heterogeneous slip as discussed before. The dislocations emitted from the crack tip move forward on the slip plane in the rising half of the fatigue cycle. In the under and peakaged conditions the fraction of the dislocations that move back is larger compared to the overaged condition since the particles are more easily cut in the former case and large numbers of dislocations are not required to destroy the strengthening effect of the particles. In other words, the slip reversibility would be higher in the under and peakaged alloy and the plastic strain accumulation would be lower for a given number of cycles. For the overaged alloys, the slip reversibility is reduced because of the larger precipitates and because the precipitate bypass mechanism is also active. This leads to a higher accumulation of plastic strain in the OA alloys for the same number of cycles and implies that for a given ΔK an overaged material would exhibit faster crack growth rates compared with lower aging conditions. A simular argument can be presented for the peakaged alloy when compared to the underaged, i.e. the strengthening precipitates are larger, they require a larger number of dislocations to destroy their strengthening effect, so slip reversibility is less than for the underaged alloy; especially at low stress intensities.

Slip reversibility differences appear to be the only logical exploration for observed difference in fatigue crack growth rates between the underaged and peakaged conditions. The trend of the fatigue crack growth rates in vacuum -- where environmental effects are minimum -- are similar to that in air suggesting that environmental degradation of crack growth resistance (38,39) in maximum slip planarity conditions is not the cause of the observed difference between the three aging conditions. However, a number of significant points should be noted about the vacuum data: (i) closure levels as compared to air decreased, (ii) crack path tortuosity and hence crack

deflections increased as compared to that in air (iii) fracture surface roughness increased. However no significant differences of these factors exist between the different aging conditions. As mentioned before the role of oxide even in air is minimal and therefore the reduction in closure due to oxide asperities in vacuum need not be considered. The other possibility could be due to fracture surface roughness. The results show that the fracture surface roughness increases considerably in vacuum with a concomitant decrease in crack closure. This suggests that the mode II displacements (40) produced due to crack path tortuosity in vacuum are reduced, or more reversible, giving rise to lower closure levels. For the 7475 alloy tested in vacuum, Carter et al. (33) showed that in spite of a major difference in the crack deflections and crack path tortuosity between the aging conditions and in different environments, the contribution from the geometrical effect of crack deflections (37) could only partially account for the differences in crack growth resistance. They suggested, as had others (33,35,36) that the extent of slip reversibility plays an important role in the fatigue crack growth rates of planar slip materials. In a vacuum environment, the slip reversibility increases due to the leak of a significant surface oxide. Thus although fractography of vacuum tested samples indicates extensive faceting it does not result in an increase of ΔK_{th}^{Cl}. The effects of mode II displacements behind the crack tip appears to be reduced in vacuum due to improved slip reversibility. Thus not only the ΔK_{th}^{Cl} is decreased but also the intrinsic crack growth resistance ΔK_{th}^{i} is increased in vacuum.

C. Fracture Toughness

One of the major goals in the development of Al-Li alloys has been to develop microstructures capable of exhibiting fracture toughness levels comparable to the 7XXX series and improvements in strength, modulus, and

density over the existing 2XXX alloys. Although several investigations have addressed the ductility problems of these alloys, very few have concentrated on the problem of fracture toughness (7,41,42). Previous investigations (3) on the fracture behavior of the Al-Li-X alloys have shown that strain localization curtails ductility in the peakaged condition. Strain localization, in conjunction with large equilibrium precipitates along boundaries, promote intergranular/intersubgranular fracture associated with wide PFZ's. Efforts to decrease the formation of the PFZ's have included chemistry modifications and deformation prior to aging. The latter process involves the introduction of dislocations which serve as sites for those precipitates that have a large coherency strain field, e.g. θ' and T_1. Recent studies by Feng et al. (7) on Al-Li-Cu alloys have shown that in the presence of Cd, deformation prior to aging might not be necessary to obtain a uniform and dense precipitation of the θ' and T_1 phases. Another beneficial effect of Cd is to slow down the growth kinetics of the strengthening precipitates by segregating to the θ'-matrix interfaces and reducing the interfacial energy (43,44). However, excessive amounts of Cd may segregate to the grain boundaries and contribute to the intergranular fracture (8).

Recrystallized and partially recrystallized structures may also be detrimental to ductility when compared with unrecrystallized structures due to secondary crack paths along the recrystallized grains (8). The suppression of recrystallization in aluminum alloys is normally attained by adding dispersoid forming elements, Cr or Mn or Zr. Of these, Zr has been observed to be the most potent in suppressing recrystallization (45). The improvement in the fracture toughness observed when adding Zr has been associated with a lesser degree of secondary cracking along the recrystallized grains (45). However, it may also be associated with the small particle size and coherent interface

when compared with Cr and Mn dispersoids. In the present work we have concentrated on the effect of the slip process on the fracture toughness. The slip process is undoubtedly controlled by the strengthening precipitates but eventually the slip dictates the fracture toughness in Al-Li-X alloys as discussed below.

The fracture toughness data collected over a wide range of aging times from compact tension specimens, are summarized in table 2. The results show decreasing fracture toughness with aging, typical of many other aluminum alloys such as 2020 (46). The accompanying change of yield stress with aging, Figure 14, shows that the K_{1C} decreases as the yield stress increases until the peakaged condition is attained beyond which the strength toughness combination decreases. A comparison of the K_{1c} values of this alloy to the commercial 2020 alloy containing Cu, Li, Mn, and Cd (Figure 14) shows that the toughness levels are comparable only at the lower aging conditions, whereas for longer aging the present alloy retains high toughness. For example, at a strength level of 475 MPa, the K_{1c} values are 35 and 20 MPa-$m^{\frac{1}{2}}$ for the present alloy and the commercial 2020 alloy, respectively. In the same Figure, K_{1c} values recently obtained for an Al-2Li-4Mg alloy (46) and a modified 2020 alloy (7) are also shown for comparison purposes.

The other mechanical property data shows that the decreasing fracture toughness is accompanied by a decrease in the strain hardening exponent and strain to fracture suggesting the possible role of these variables on the fracture toughness, as will be discussed later. Extensive fractography of the fracture toughness samples revealed transgranular slip band fracture and secondary cracking along grain boundaries, in both under and peakaged, Figure 15a, and (b), some very rare occurrence of transgranular microvoid

coalescence, Figure 15c, and ductile intergranular failure in the overaged microstructure, Figure 15d.

The major transgranular slip band fracture mechanism in the underaged to peakaged conditions was found to occur over several microns ahead of the crack tip. These observations suggest that the slip bands emanating from the crack tip have often extended unimpeded transgranularly across many subgrains and possibly several grains. This is due to the low misorientation between subgrains and the sharp deformation texture of the plate. Some transgranular microvoid coalescence associated with iron and silicon constituents as shown in the micrograph of Figure 15c was rare and did not appear to control the overall fracture. The major mechanism of fracture for the overaged conditions, Figure 15d, shows the presence of small microvoids along grain boundaries suggesting a ductile intergranular type of failure, associated with a weakening of the grain boundaries in the overaged conditions. Starke, Sanders and Palmer (3) suggest that for Al-Li alloys the slip bands impinging on the grain boundaries transfer the strain to the soft PFZ's along the grain boundaries. These regions deform with ease and hence strain is localized here, giving rise to a more easily attainable fracture route along the grain boundaries.

Many investigations in the past have shown that a relationship between the strain hardening exponent obtained in uniaxial tension tests and K_{1c} exist (47,48,49). Recently, Garret and Knott (47) have shown that the critical crack opening displacement at the onset of crack extension is proportional to the square of the strain hardening exponent for a constant ductile fracture strain, thus suggesting that the K_{1c} is proportional to the strain hardening exponent. The dependence of K_{1c} on the strain hardening exponent for the Al-Cu-Li alloy under study is suggested by the micrographs of Figure 16, taken

after unloading the compact tension samples at the onset of crack extension. These micrographs illustrate that, in the underaged condition the plastic zone wings are wider than in the peakaged condition. Gerberich (50) and Hahn and Rosenfield (51) showed for a number of alloy systems, including aluminum alloys that the plastic zone width, D, is proportional to the square of the strain hardening exponent, n given as

$$D(n) = 0.0013 + 2.54\ n^2 \text{ (cm)} \qquad (2)$$

Due to the dispersion of the plasticity, the crack tip in the underaged condition experiences a lower strain concentration than in the peakaged condition for a given load level. Thus the load bearing capacity in the presence of a notch is higher in the underaged conditions. If the crack extension is considered to occur after a critical strain has accumulated or when the strain hardening capacity is exhausted then the underaged samples would exhibit a higher fracture toughness.

This qualitative relationship between the fracture toughness and the strain hardening exponent does not, however, offer an explanation at a microscopic level, since the plastic zones in front of the crack tip include the plasticity in intense slip bands as well as the plasticity between the bands. In order to incorporate microstructural features and the process zone it might be necessary to consider the extent of strain localization which is controlled by the character of the strengthening precipitates.

Going from the underaged to peakaged condition, the fracture toughness is limited by the slip band decohesion process without the involvement of any void growth. This process is considered to occur when a critical displacement or strain is reached in some potential slip bands in front of the crack tip. A similar criterion has been discussed in detail by Smith, Cook and Rau (52) for materials exhibiting strain localization. The analysis here is different

in that the macroscopic shear fracture is related to the local plasticity in the slip bands where the degree of localized plasticity as observed increases with degree of aging till the peakage condition is reached.

We have approached this problem by considering slip on planes inclined to the crack plane at an angle α (53,54). In such a situation the vertical displacements in two symmetric slip bands produced by N dislocations in front of the crack tip having similar Burgers vector b, would be 2 (Nb) Sin α. This displacement in the front of the crack tip would then be accommodated by the vertical crack tip opening displacement δ, leading to

$$\delta = 2\ (Nb)\ \text{Sin}\ \alpha \tag{3}$$

The dislocations in front of the crack tip may be homogeneously distributed throughout the plastic zone and some may be concentrated in intense slip bands that lie within the plastic zone. Consequently, δ may be the sum of these contributions

$$\delta = 2[(N)_u b + (N)_{SB} b]\ \text{Sin}\ \alpha \tag{4}$$

where $(N)_u$ b represents the displacement due to homogeneous slip and $(N)_{SB}$b represents the displacement in the slip bands. The relative magnitude of each contribution would be dependent on the aging conditions since the tendency for strain localization increases as aging progresses up to the peakaged condition. Only those dislocations in the intense slip bands should be considered to contribute to the critical strain that is necessary for transgranular slip band fracture. The density of these dislocations may be defined as

$$\rho_{SB} = (N)_{SB}/LW \tag{5}$$

where W is the slip band width and L the slip band length. Following Orowan, the shear strain in the slip band may be written as

$$\gamma_{SB} = \rho_{SB} bL$$
$$= \frac{(N)_{SB}}{LW} \cdot bL = (N)_{SB} b/W \qquad (6)$$

A critical value of γ_{SB} would be necessary for fracture to occur. As aging progresses a smaller δ is required to reach the critical strain since, for a given δ, $(N)_{SB}$ increases and W decreases with aging. We may express δ in terms of the stress intensity factor, K, the yield stress, σ_{ys}, and Young modulus, E, by the relationship (55)

$$\delta = \frac{0.5K^2}{E\sigma_{ys}} \qquad (7)$$

Substituting for δ and ignoring the contributions of those dislocations that are homogeneously distributed, we obtain

$$\frac{0.5K^2}{E\sigma_{ys}} = (2 \text{ Sin } \alpha \ \gamma_{SB} W) \qquad (8)$$

Initial crack extension occurs when γ_{SB} reaches a critical value, γ^c_{SB}, and the fracture toughness may be expressed as

$$K_{1c} = \left[4E\sigma_{ys} \ \gamma^c_{SB} \ W \text{ Sin } \alpha\right]^{\frac{1}{2}} \qquad (9)$$

This equation has been obtained for two symmetric slip bands at the crack tip. However, the equation needs to be modified to take into consideration the number of active slip bands which would be determined by the plastic zone width (D) and the slip band spacing (d). The modified equation then reads as

$$K_{1c} = \left[S \text{ Sin } \alpha \ E\sigma_{ys} W \left(\frac{D}{d}\right) \gamma^c_{SB}\right]^{\frac{1}{2}} \qquad (10)$$

The value of $\frac{D}{d}$ in the peak aged condition from measurements of slip band spacing and etched plastic zone width comes out to be 39. Measured values for other aging conditions were employed in the above equation. The number of active slip bands in front of the crack tip decreases due to higher strain localization as aging increases. The critical strain for fracture was assumed to be either 1/3 (plane strain) or 1/2 (plane stress) of the tensile fracture ductility of the as-quenched specimen, 0.46. The rationale behind this, is that the loss in ductility and fracture toughness in aged specimens is due to the attainment of the same strain as that of the as-quenched specimen but in localized slip bands. So, with increasing degree of flow localization the same strain is concentrated in lesser number of slip bands causing fracture to be attained earlier than when the slip is not so localized. The factors 1/2 and 1/3 are taken from Hahn and Rosenfield (51) which essentially account for the plane strain and plane stress ductility situations in notched specimens.

The model predicts the correct trend of the fracture toughness variation with yield strength, Figure 17. Experimental fracture toughness values of an Al-2.1Li-2.9Cu-0.12Zr alloy, obtained by Vasudevan and Suresh (42) are also shown in Figure 17. The application of the present model to their fracture toughness data is justified based on the similarity in composition and deformation mode with our alloy. Calculated slip band spacings from Vasudevan and Suresh's micrographs for their UA-1, PA, and OA-1 are 3.12, 6.7, and 3.17 microns respectively, suggesting increasing slip localization from underaged to peakaged and then a return to less localized slip in the overaged condition, similar to the trend we observed, Figure 6. The width of their slip bands could not be measured with accuracy because of the orientation of the sample and the limited resolution of their scanning electron micrographs. As confirmed by our experimental observations and those of Dowling and Martin

(58) and Evenson et al (59), increasing slip band spacing is accompanied by decreasing slip band widths in aluminum alloys (coarse slip refers to small slip band width). We can therefore assume that the slip band width would be a minimum in the peakaged condition of their alloy based on the above findings and also on their observation that the coarsest slip was observed for the peakaged condition. Further evidence of the similarities in the deformation mode of the two alloys is exemplified by the trend in yield stress, strain hardening exponent and fracture ductility values, with aging (60). Our model is based on deformation mode (slip band spacing and width) and since similarities in the slip process between two alloys exist, it is appropriate to make a comparison of their fracture toughness values to the predictions of our model for their underaged alloys for which crack extension occurs by transgranular slip band fracture. The higher aging temperature used in their study most likely resulted in extensive grain boundary precipitation in the peakaged condition (60) This enhanced grain boundary fracture and it was, therefore, inappropriate to compare their peakaged fracture toughness value to the prediction of our model since the model is concerned with transgranular fracture along slip bands. The present analysis suggests that the fracture toughness decreases with increasing yield strength due to a decreasing slip band width and increasing slip band spacing. This is shown schematically in Figure 18. The predicted values are slightly lower at peakaged and higher in the underaged microstructures, Figure 17.

Several investigators (56,57) have examined the problem of ductile fracture strain under different states of stress. Such experiments are currently underway to obtain a better correlation between the slip band width and spacing to the fracture strains in notched tensile specimens.

The behavior of the newly developed Al-Li-X alloys is different from most other aluminum alloys in that the characteristic fracture associated with void initiation at constituent particles and coarse incoherent Mn and Cr dispersoids and the subsequent void growth by shear localization is absent. The volume fraction and size of these particles is low due to the extremely low contents of Fe and Si, Table 1 and the use of Zr as the dispersoid forming element. Previous work (7) on Al-Li-Cu alloys containing higher Fe and Si contents suggest that coarse constituent particles aid in fracture initiation via microvoid nucleation at these particles and decrease ductility. The Cr and Mn dispersoids may homogenize slip in aluminum alloys and thus, increase the work hardening exponent. However, the detrimental nature of the large Mn and Cr containing particles on the fracture ductily is clearly demonstrated in the literature (45). Microvoids are normally not associated with the small coherent Al_3Zr dispersoids.

Conclusions

The Al-Li-Cu alloy studied exhibits comparable strength and ductility levels to commercial high strength Al alloys. The yield strength in the peakaged condition is 520 MPa and is accompanied by an 8 percent elongation. The strength increase is, however, accompanied by strain localization which curtails ductility. The general trend of increasing fatigue crack growth resistance with lower aging time remains after considering both crack closure and crack deflections. The fracture toughness in the peakaged condition is 32 MPa $m^{\frac{1}{2}}$. This value together with yield strength compares well with the currently available data on 2XXX and 7XXX alloys. It has been demonstrated that increasing slip localization accompanied by decreasing strain hardening exponent results in a decreasing fracture toughness through a critical strain accumulation at the crack tip needed for the initial crack extension.

Acknowledgements

This research was sponsored by the Air Force Office of Scientific Research, United States Air Force Systems Command, under Grant AFOSR-83-0061, Dr. Alan Rosenstein, program manager. The authors would like to thank Prof. K. Lawless and Mr. W. Cassada for valuable discussions and experimental assistance.

References

1. J. S. Ekvall, J. E. Rhodes, and G. G. Wald: in Design of Fatigue and Resistant Structures, ASTM STP 761, 1982, p. 328.

2. W. E. Quist, G. H. Harinarayanan, and A. L. Wingert: in Aluminum-Lithium Alloys II, E. A. Starke, Jr., and T. H. Sanders, Jr., eds., TMS-AIME, Warrendale, PA, 1984, p. 313.

3. E. A. Starke, Jr., T. H. Sanders, Jr., and I. G. Palmer: J. of Metals, 1981, Vol. 33, No. 8, p. 24.

4. W. S. Miller, A. J. Cornish, A. P. Tichener, and D. A. Bennet: in Aluminum-Lithium Alloys II, E. A. Starke, Jr., and T. H. Sanders, Jr., eds., TMS-AIME, Warrendale, PA, 1984, p. 355.

5. T. H. Sanders, Jr., and E. A. Starke, Jr., eds., Aluminum-Lithium Alloys, TMS-AIME, 1981.

6. E. A. Starke, Jr., and T. H. Sanders, Jr., eds., Aluminum-Lithium Alloys II, TMS-AIME, Warrendale, PA, 1984.

7. W.X. Feng, F.S. Lin, and E.A. Starke, Jr.: Metall. Trans. A, 1984, 15, p. 1209.

8. E. A. Starke, Jr. and F. S. Lin: Metall. Trans. A, 1982, 13A, p. 2259.

9. B. Noble and G. E. Thompson: Metal Science Journal, 1971, 5, p. 114.

10. B. Noble and G. E. Thompson: Metal Science Journal, 1972, 6, p. 167.

11. K. Schneider and M. Von Heimendahl: Z. Metallkde, 1973, 64 (5), p. 342.

12. F. W. Gayle and J. B. Van der Sande: Scr. Met. 1984, Vol. 18, p. 473.

13. P. Hirsch, A. Howie, R. B. Nicholson, D. W. Pashley, and M. J. Whelan, in Electron Microscopy of Thin Crystals, R.E. Kreiger Publishing Co., 1977, p. 336.

14. C. Laird and H. I. Aaronson: Trans. TMS-AIME, 1968, 242, p. 1393.

15. J. M. Silcok, J. Inst. Met. 1959-60, Vol. 80, p. 357.

16. B. Noble, I. R. McLauchlin, and G. Thompson, Acta Met., 1970, Vol. 18, p. 339.

17. P. J. Gregson and H. M. Flower: Acta Met., 1985, 33(3), p. 532.

18. S. Cersora, G. Cocco, G. Fayherazzi and L. Schiffini, Phil Mag. 35, p. 373 (1977)

19. T. H. Sanders and E. A. Starke, Acta Met. 1982, 36, p. 927.

20. H. Gleiter and E. Hornbogen, Mat. Sci. Engr. 1967/68, vol. 2, p. 285.

21. H. Gleiter and E. Hornbogen, Phys. Stat. Sol. 1965, vol. 12, p. 235.

22. E. Hornbogen and K. H. Zum Gahr, Metallography, 1975, vol. 8, p. 181.

23. G. Lutjering and S. Weissman, Acta Met. 1970, vol. 18, p. 785.

24. E. Hornbogen and G. Lutjering, 6th Intern. Conf. on Light Metals, Leoben/Vienna, Aluminum Verlag Dusseldorf, 1975, p. 40.

25. A. Gysler, G. Lutjering, and V. Gerold, Acta Met. 1974, vol. 22, p. 901.

26. G. Terlinde and G. Lutjering, Met. Trans. A, vol. 13A, 1982, p. 1283.

27. P. M. Kelly, Inter. Met. Rev., 1973, vol. 18, p. 31.

28. E. Hornbogen: in Strength of Metals and Alloys, R. C. Gifkin ed., ICSMA 6, 1982, Vol. 3, p. 1059.

29. C. J. Beevers: in Fatigue Thresholds, Fundamentals and Engineering Applications, J. Backlund, A. F. Blom, and C. J. Beevers, eds., Engineering Materials Advisory Services, Ltd., West Midlands, UK, 1981, Vol. 1, p. 257.

30. S. Suresh: Brown University, Private Communications.

31. J. Petit, B. Bouchet, C. Goss and J. de Fouguet: Fracture, Proceedings 4th Int. Conf. on Fracture (ICF4) D. M. R. Taplin, ed., University of Waterloo Press, Waterloo, Canada, 1977, Vol. 2, p. 687.

32. A. K. Vasudevan, P. E. Bretz, A. C. Miller, and S. Suresh: Mater. Sci. and Eng. 1984, 64, p. 113.

33. R. D. Carter, E. W. Lee, E. A. Starke, Jr., and C. J. Beevers: Metall. Trans. A, 1984, Vol. 15A, p. 555.

34. R. L. Donahue, H. M. Clarke, P. Antanio, R. Kumble, and A. J. McEvily: Inter.J. of Fract. Mech., 1972, 8, p. 209.

35. J. Lindigkeit, G. Terlinde, A. Gysler, and G. Lutjering: Acta. Metall.1979, vol. 27, p. 1717.

36. E. Hornbogen and K-H. Zum Gahr: Acta. Metall. 1976, vol. 24, p. 581.

37. S. Suresh: Metall. Trans., 1985, vol. 6A, p. 249.

38. H. A. Hall: Corrosion, June, 1967, p. 175.

39. S. Suresh, A. K. Vasudevan and P. E. Bretz: Metall. Trans. A, 1984, Vol. 15A, p. 369.

40. S. Suresh and R. O. Ritchie: Metall. Trans. A, 1982, Vol. 13A, p. 1627.

41. F. S. Lin, S. B. Chakrabortty and E. A. Starke, Jr.: Metall. Trans. A, 1982, 13A, p. 401.

42. A. K. Vasudevan and S. Suresh, Mater. Sci. and Eng., 1985, Vol. 72, p. 37.

43. J. M. Silcock, T. J. Heal and H. K. Hardy: J. Inst. of Met., 1955-56, 84, p.23.

44. J. D. Boyd and R. B. Nicholson: Acta Met. 1971, 19, p. 1979.

45. J. T. Staley: Properties Related to Fracture Toughness, W. R. Warke, V. Weiss and G. T. Hahn, eds., ASTM STP 605, ASTM 1975, p. 71.

46. S. J. Haris, K. Dinsdale, B. Noble: in Al-Li Alloys II, E. A. Starke, Jr., and T. H. Sanders, Jr., eds., TMS-AIME, Warrendale, PA.

47. G. G. Garret, and J. F. Knott: Metall. Trans. A., 1978, Vol. 9A, p. 1187.

48. G. T. Hahn and A. R. Rosenfield: Metall. Trans. A, 1975, 6A, p. 653.

49. J. G. Rinker, M. Marek and T. H. Sanders, Jr.: in Aluminum-Lithium Alloys, E. A. Starke, Jr., and T. H. Sanders, Jr., eds. TMS-AIME, Warrendale, PA, p. 597, 1984.

50. W. W. Gerberich: Experimental Mechanics 1964, Vol. 4, p. 335.

51. G. T. Hahn and A. R. Rosenfield: ASTM STP 432, 1968, p. 27.

52. E. Smith, T. S. Cook and C. A. Rau: Fracture, Proc. 4th Int. Conf. on Fracture (ICF4), D. M. R. Taplin, ed., University of Waterloo Press, Waterloo, Canada, 1977, Vol. 1, p. 215.

53. Johaness Weertman: in Fatigue and Microstructure, M. Meshii, ed. American Society for Metals, Metals Park, Ohio, 1979, p. 279.

54. V.Vitek: J. Mech. Phys. Solids, 1976, Vol. 24, p. 263.

55. J. F. Knott: in Fundamentals of Fracture Mechanics, Butterworths & Co. (Publishers) Ltd. London, UK, 1973.

56. R. O. Ritchie, W. L. Server and R. A. Wullaert: Metall. Trans. A, 1979, 10A, p. 1557.

57. R. O. Ritchie and A. W. Thompson: Metall. Trans. A, 1985, 16A, p. 233.

58. Judith M. Dowling and J. W. Martin, Acta Met. 1976, Vol. 24, p. 1147.

59. J. D. Evensen, N. Ryum and J. D. Embury, Mat. Sci. Engr., 1975, Vol. 18, p. 221.

60. R. F. Ashton, D. S. Thompson, E. A. Starke, Jr., and F. S. Lin, "Processing of Al-Li-Cu-(Mg) Alloys," Proceeding of the Gluril International Conference ond Aluminum-Lithium Alloys," Oxford, England, August, 1985 (in press).

TABLE 1

Actual Chemical Composition in Weight Percent

Cu	Li	Cd	Zr	Fe	Si	Al
3.6	1.68	0.16	0.16	0.01	0.02	bal.

TABLE 2

Mechanical Properties

Microstructure	Aging time	σ_{ys} (MPa)	σ_{uts} (MPa)	% elongation*	n	$^{+}\varepsilon_f^T$	K_{1c}
UA-1	8 hrs.	300	431	20	0.13	0.3568	44
UA-2	12 hrs.	350	452	18	0.098	0.315	40
PA	17 hrs.	520	534	8	0.055	0.145	32.2
OA-1	19 hrs.	500	526	8.6	0.062	-	30
OA-2	22 hrs.	484	500	6.6	0.056	-	27
OA-3	26 hrs.	472	496	4.0	0.062	-	30

*as measured on 19 mm gage length

$^{+}\varepsilon_f^T = \ln\left(\frac{A_o}{A_f}\right)$; A_o is the original and A_f is the final cross sectional area.

TABLE 3

Fatigue Threshold Stress Intensities

Microstructure	Environment	ΔK_{th} Mpa $m^{\frac{1}{2}}$	ΔK^{i}_{th} Mpa $m^{\frac{1}{2}}$	ΔK^{Cl}_{th} Mpa $m^{\frac{1}{2}}$
UA-2	Air	3.7	3.1	0.6
PA	Air	2.8	2.4	0.4
OA-2	Air	2.3	2.3	negligible
UA-2	Vacuum	5.5	5.3	0.2
PA	Vacuum	4.3	4.0	0.3
OA-2	Vacuum	3.6	3.4	0.2

$$\Delta K_{th} = \Delta K^{observed}_{th} \text{ or } \Delta K^{apparent}_{th}$$

$$\Delta K^{i}_{th} = \Delta K_{th} - \Delta K^{Cl}_{th}$$

$$\Delta K^{Cl}_{th} = K^{Cl}_{th} - K^{min}_{th}$$

TABLE 4

Measured Deformation Parameters

Microstructure	Slip band width W	Slip band Spacing d	Plastic zone width D
	(μm)	(μm)	(μm)
UA-1	0.4	0.5	442
UA-2	0.31	1.33	256
PA	0.256	2.516	90
OA-2	0.61	2.166	-

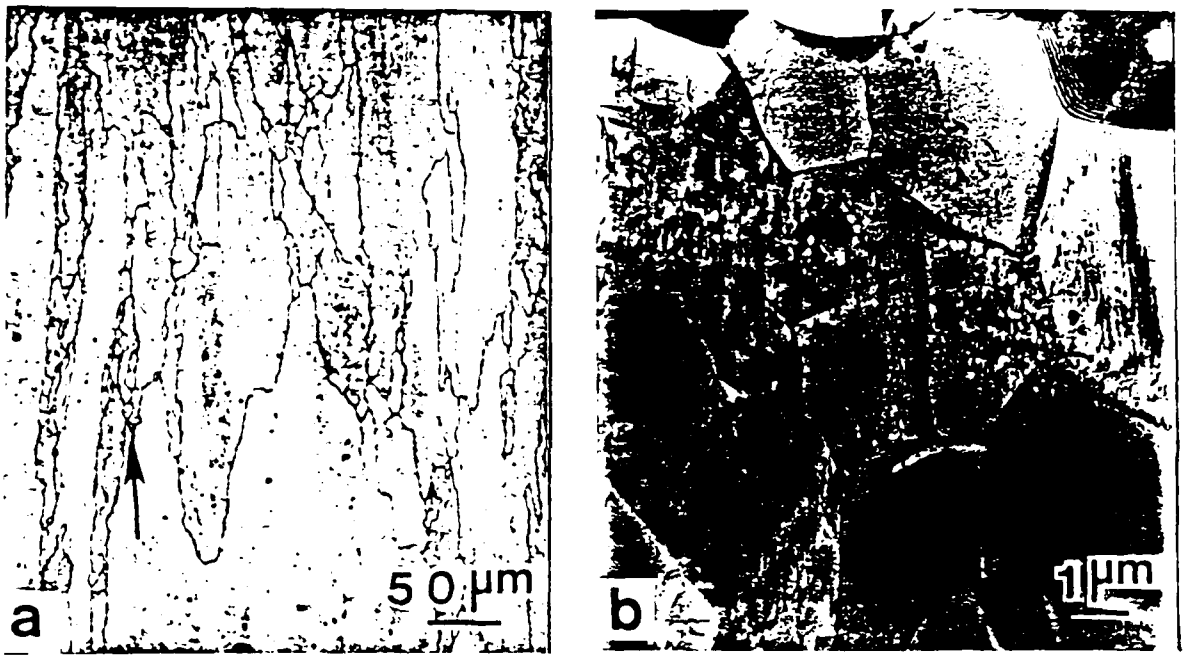

Figure 1: (a) Optical micrograph of the L-S section illustrating the large unrecrystallized grains and small recrystallized grains (shown by arrow) formed during the solution heat treatment, and (b) TEM of the subgrain structure in the {112} foil plane.

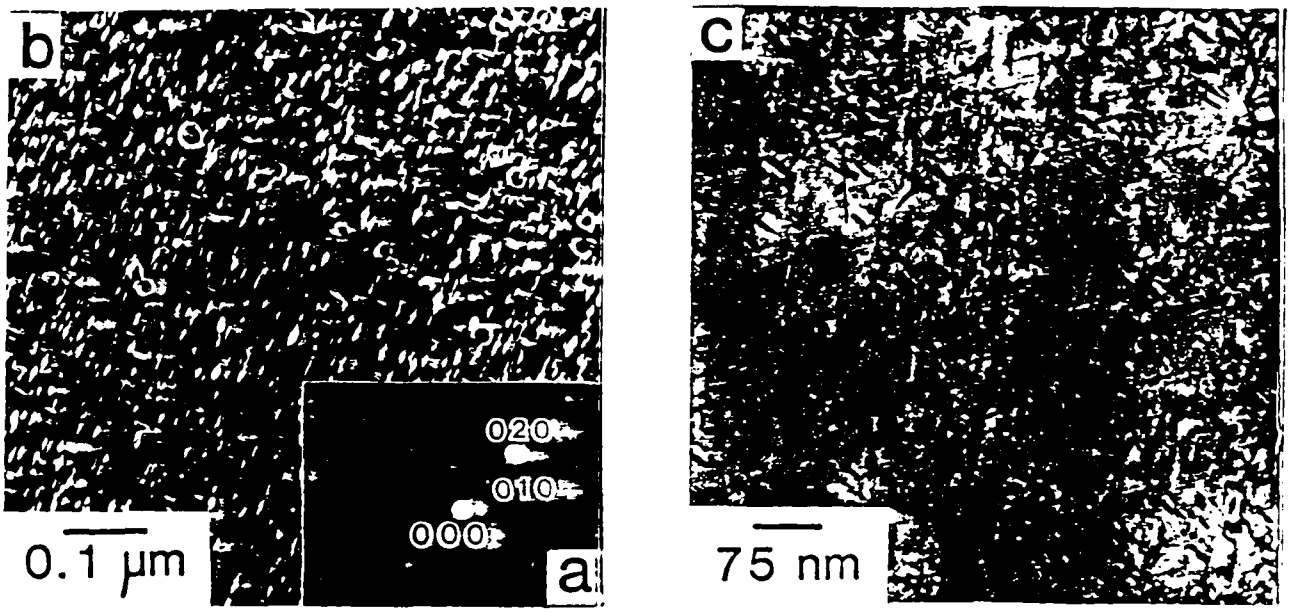

Figure 2: (a) Diffraction pattern of UA-2 showing the Al_3 Li-Al_3Zr superlattice spot and the streak corresponding to Al_2Cu precipitates. (b) DF image showing the three variants of Al_2Cu precipitates. Note the Al_3Zr precipitates. (c) BF of 0' and T_1 precipitates in the {112} foil plane in PA.

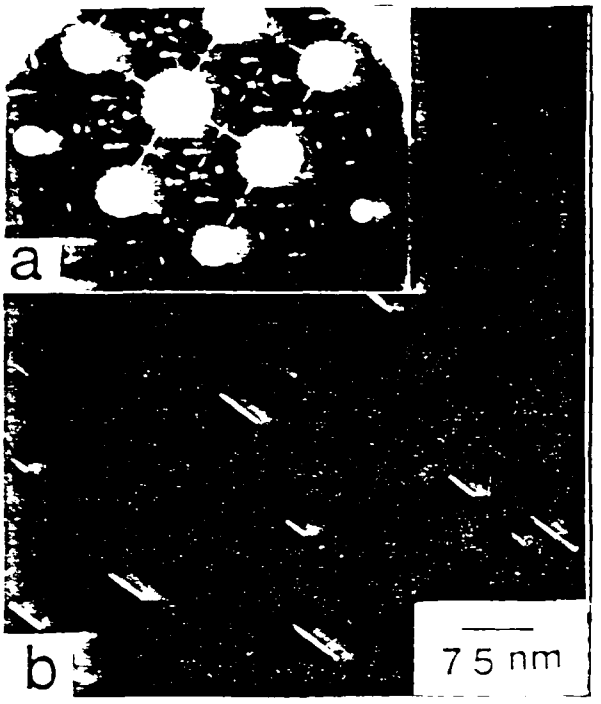
a
b
75 nm

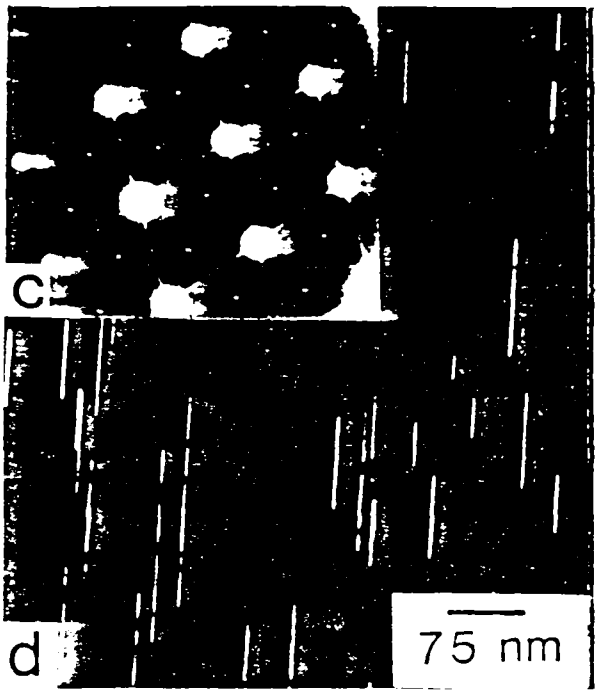
c
d
75 nm

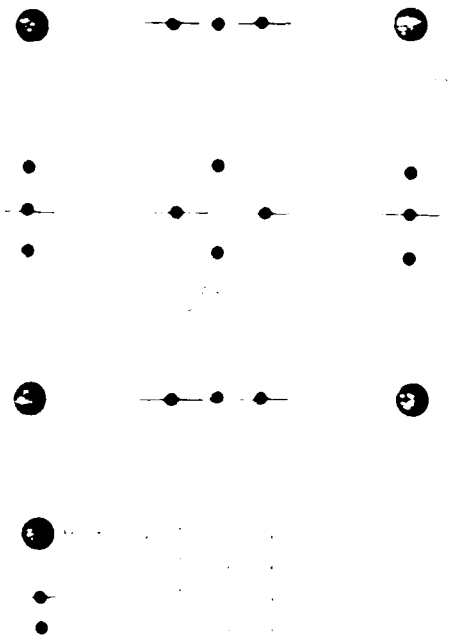

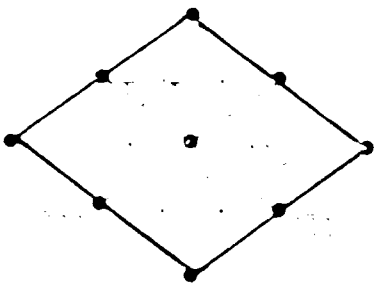

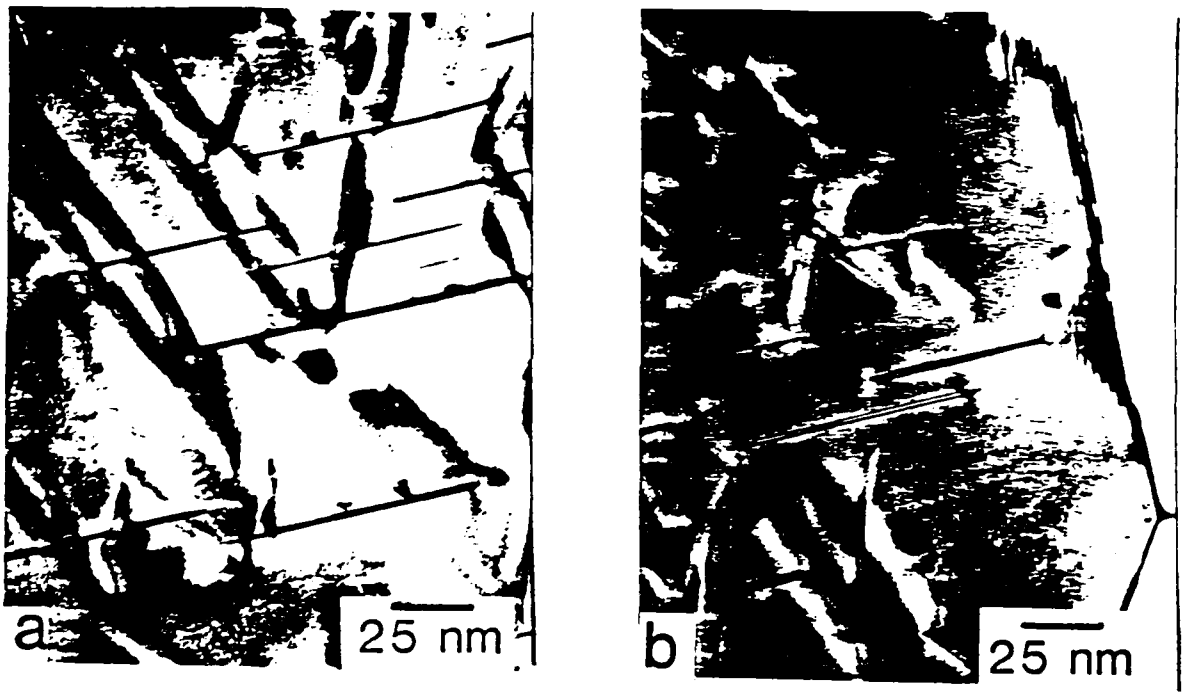

Figure 4: BF images in the overaged condition with (a) g = 220; (b) g = 220. Sample aged at 160°C for 40 hours.

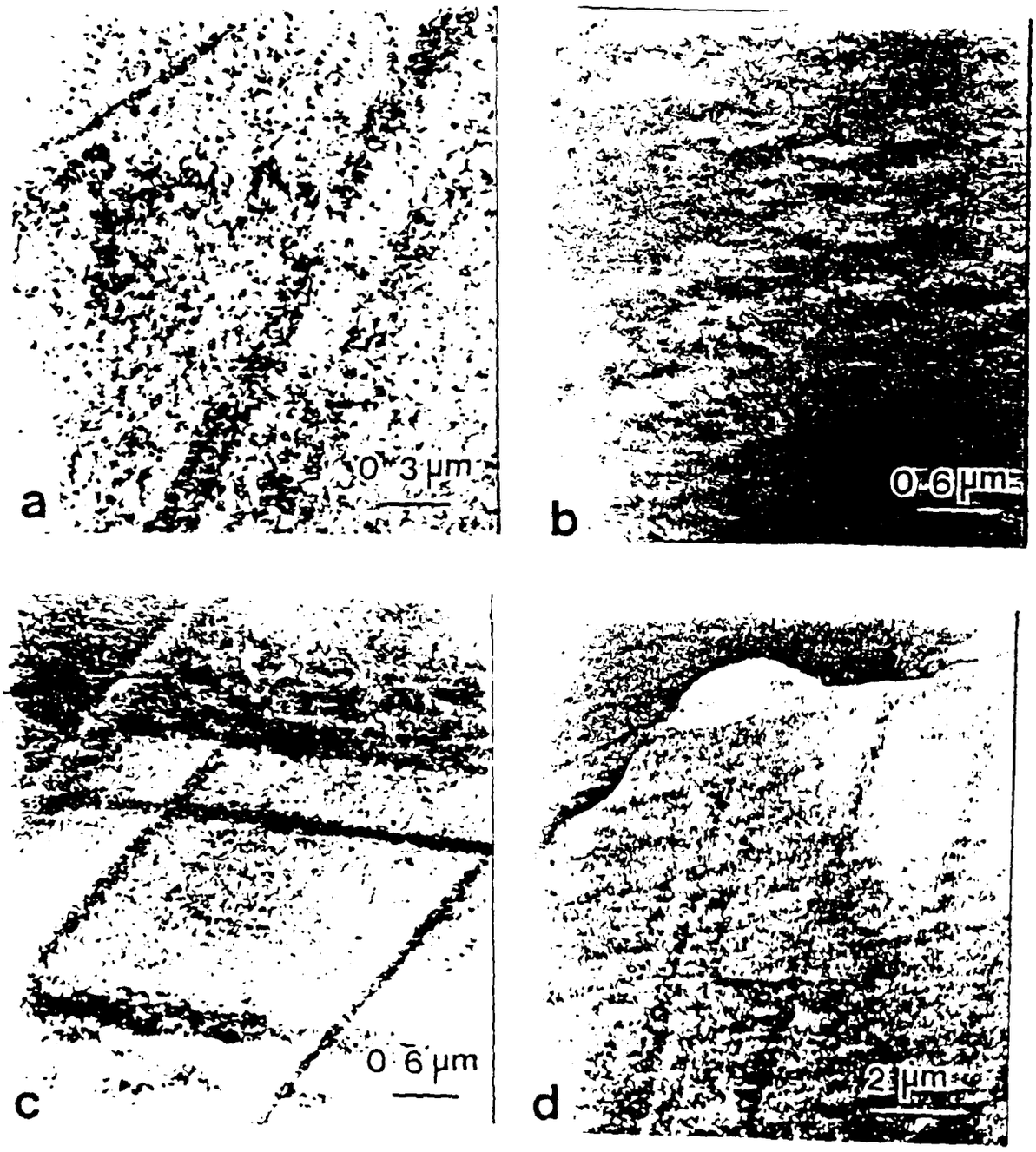

Figure 5: Bright field TEMs with <110> zone axis illustrating the planar slipbands in fractured tensile specimens aged at 434K for (a) 0 hours (b) 10 hrs., (c) 17 hrs., and (d) 22 hrs; g = 220

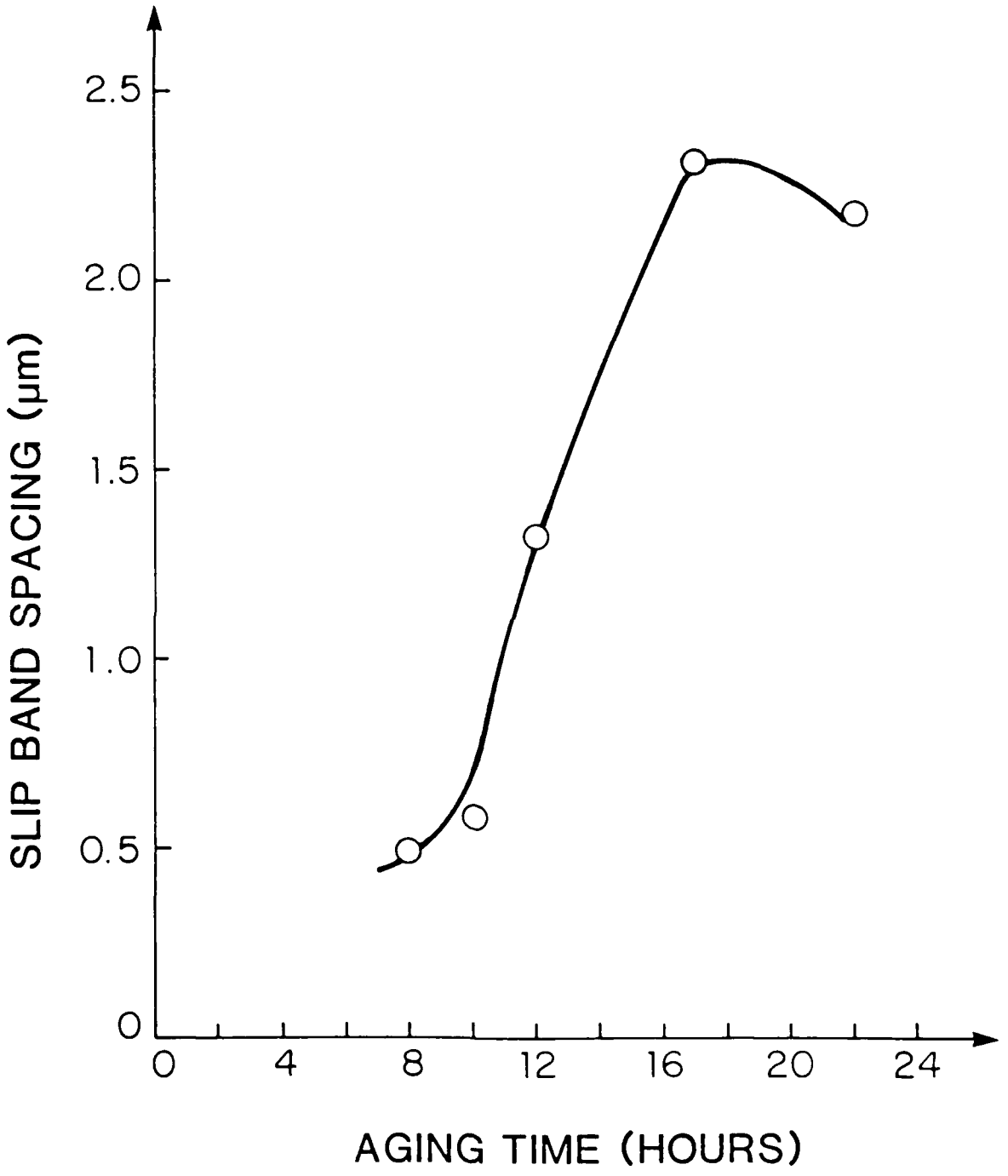

Figure 6: Variation of slip band spacing with aging time.

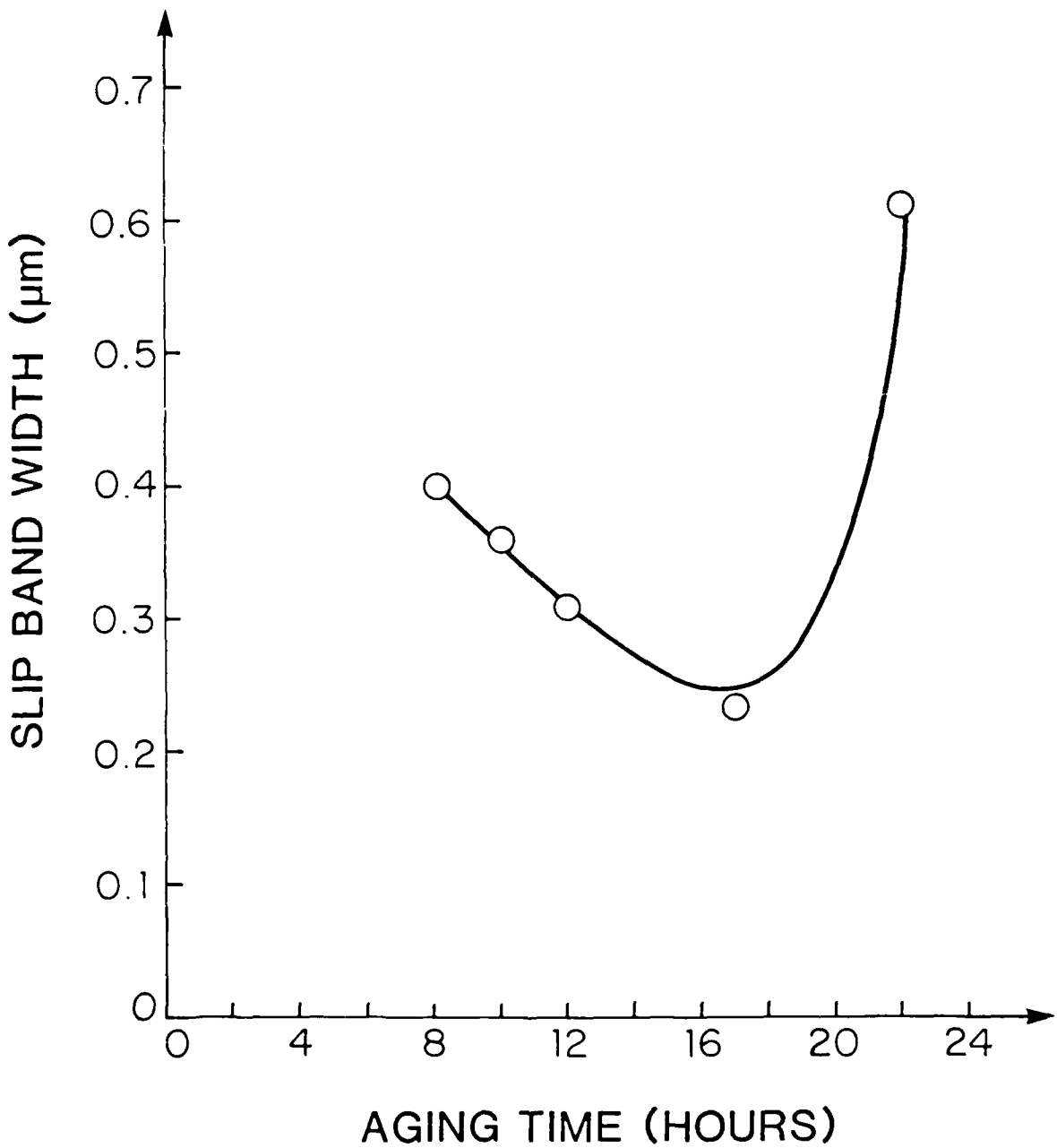

Figure 7: Variation of slip band width with aging time.

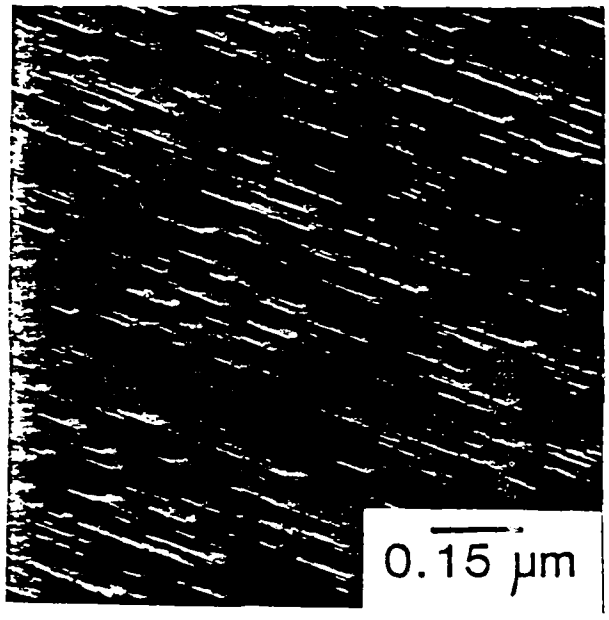

Figure 8: (a) DF micrograph showing the T_1 shearing in OA-2 imaged with the T_1 streak, zone axis near [110], (b) BF micrograph showing dislocation bypassing T_1. Zone axis near [110]; g = 220.

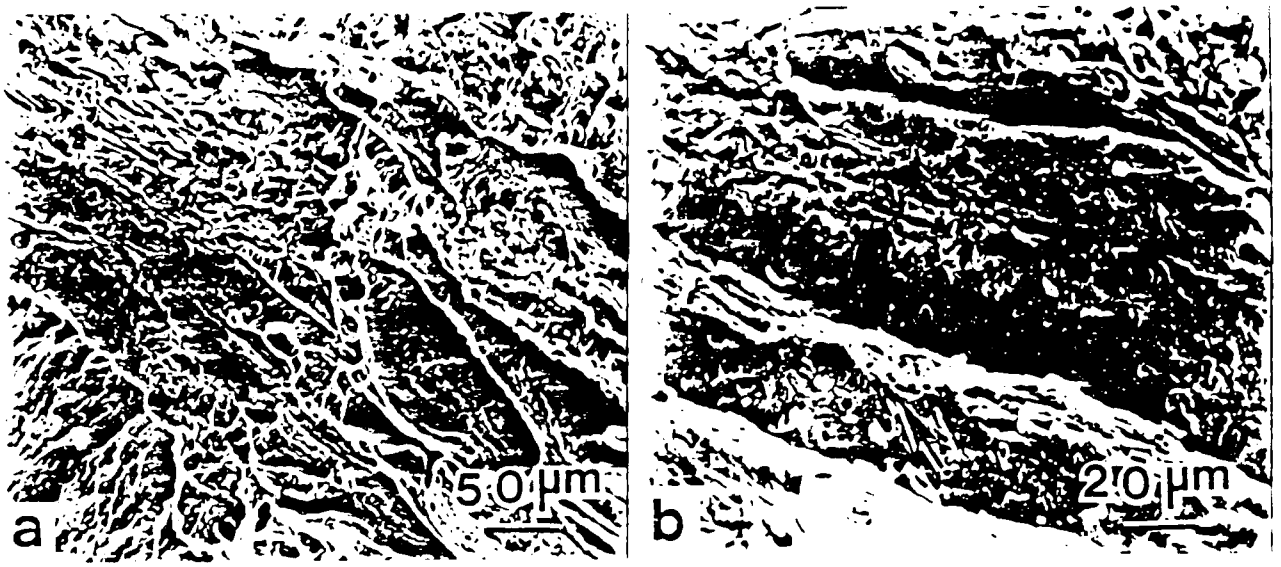

Figure 9: SEM micrographs of the transgranular shear fracture in tensile testing (a) underaged conditions (b) overaged conditions. Secondary cracking and voids associated with equilibrium precipitates (shown by arrow) are observed in condition (b).

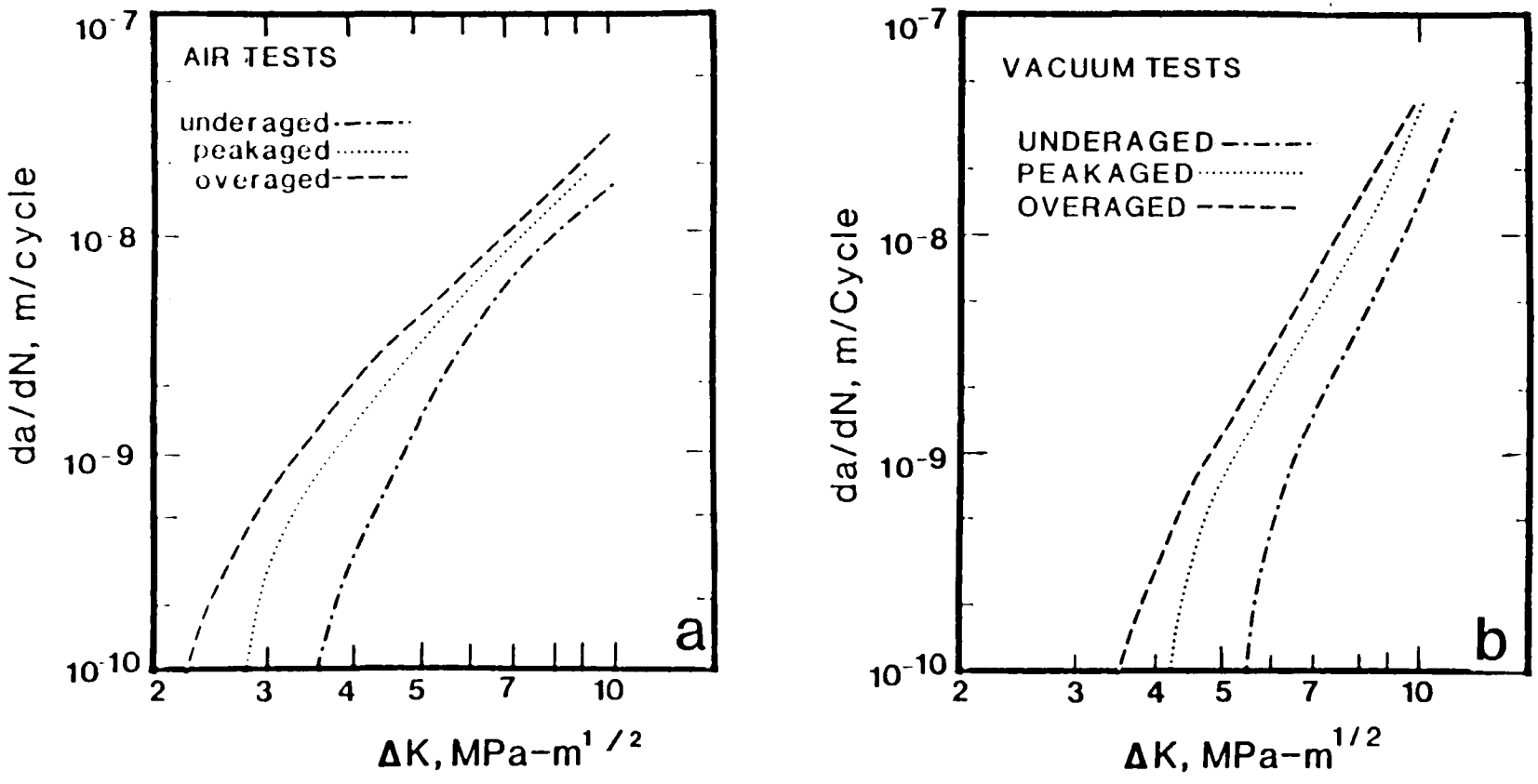

Figure 10: Fatigue crack growth rates of the microstructural variants tested in (a) laboratory air (R.H. of 45 percent) and (b) vacuum (10^{-5} torr).

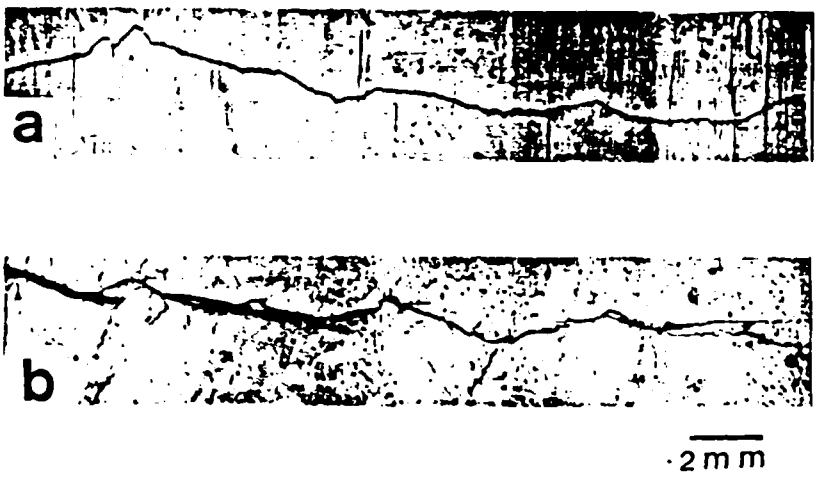

Figure 11: Optical micrographs of the crack profile of the fatigue crack propagation samples tested in air (a) underaged condition and (b) overaged condition.

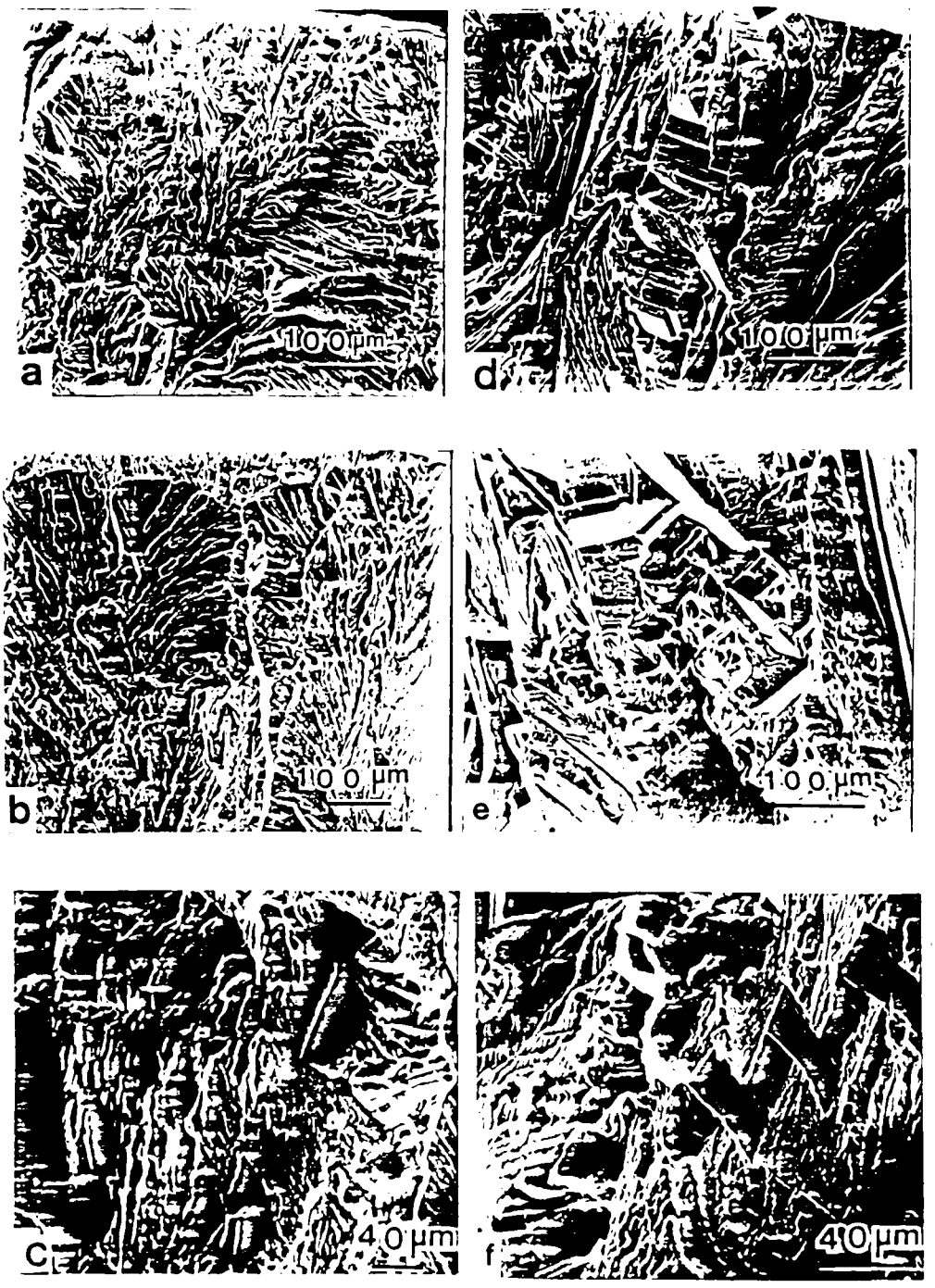

Figure 12: Fractography associated with fatigue crack propagation near threshold (a) UA-2 tested in air, (b) peakaged tested in air (c) OA-2 tested in air, (d) UA-2 tested in vacuum, (e) PA tested in vacuum, (f) OA-2 tested in vacuum.

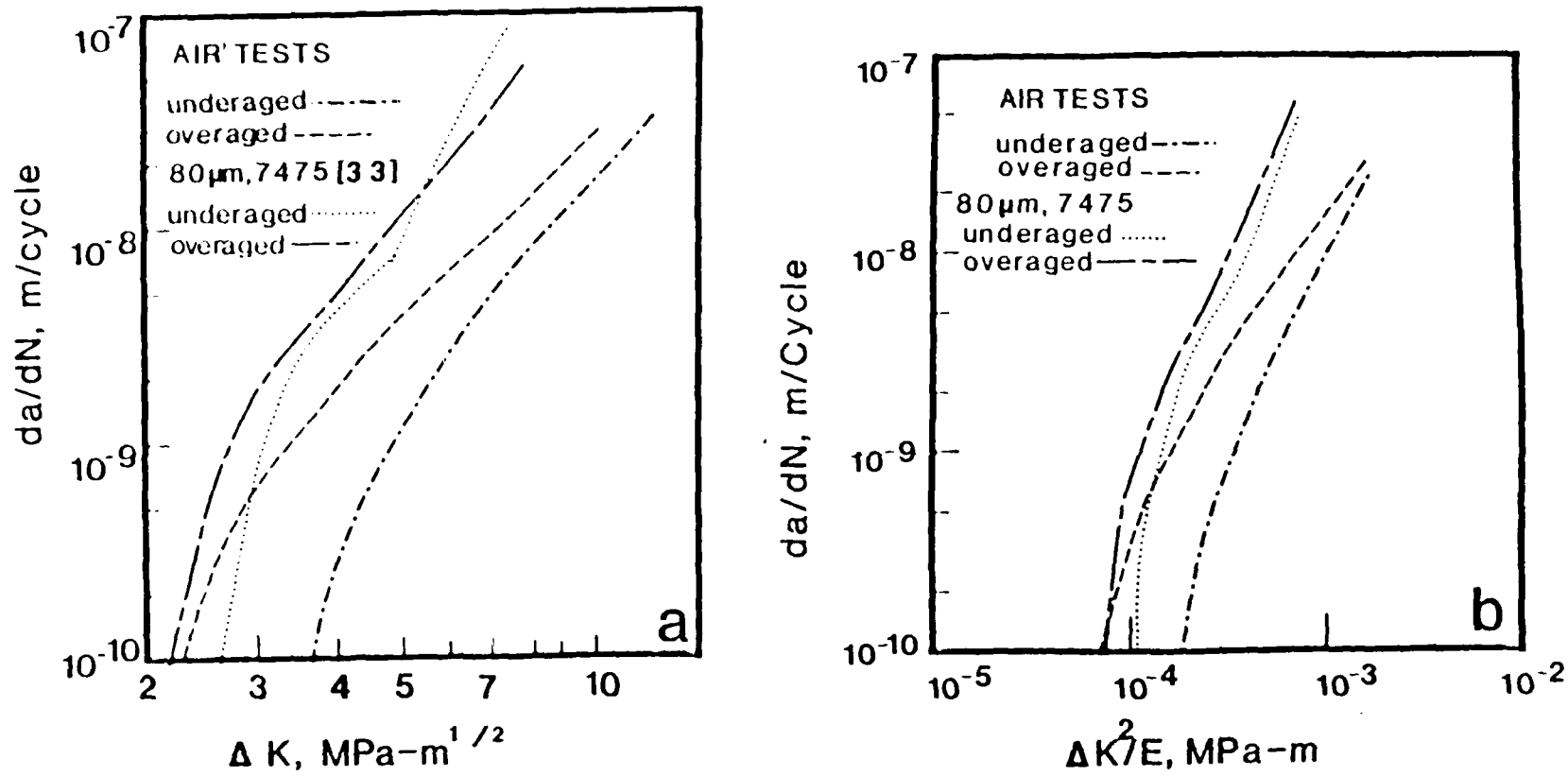

Figure 13: A comparison of the fatigue crack growth rates of the present alloy with thermomechanically processed 7475 alloy as a function of (a) ΔK and (b) as a function of normalized ΔK^2 with respect to Young's modulus E.

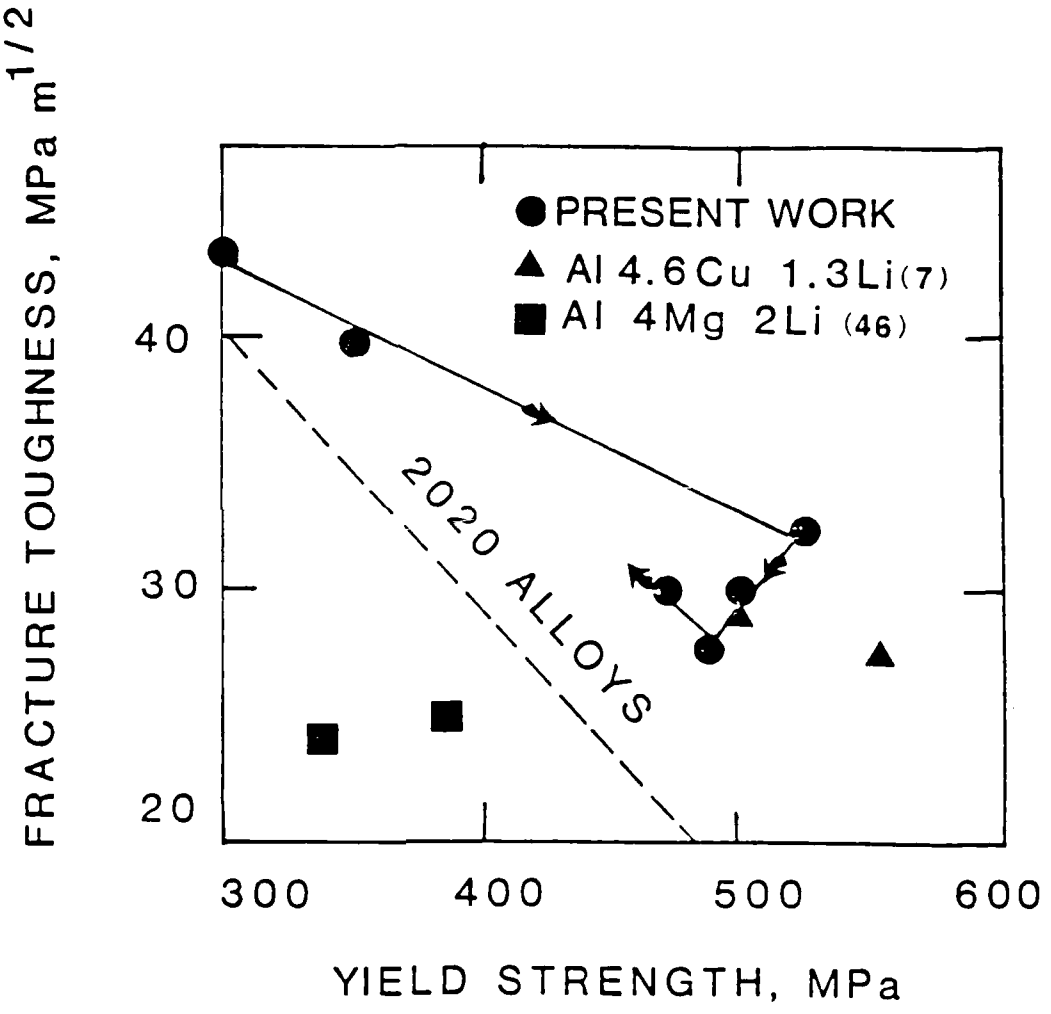

Figure 14: Variation of fracture toughness with yield strength for the present alloy and a comparison to the data of other Al-Li-X alloys.

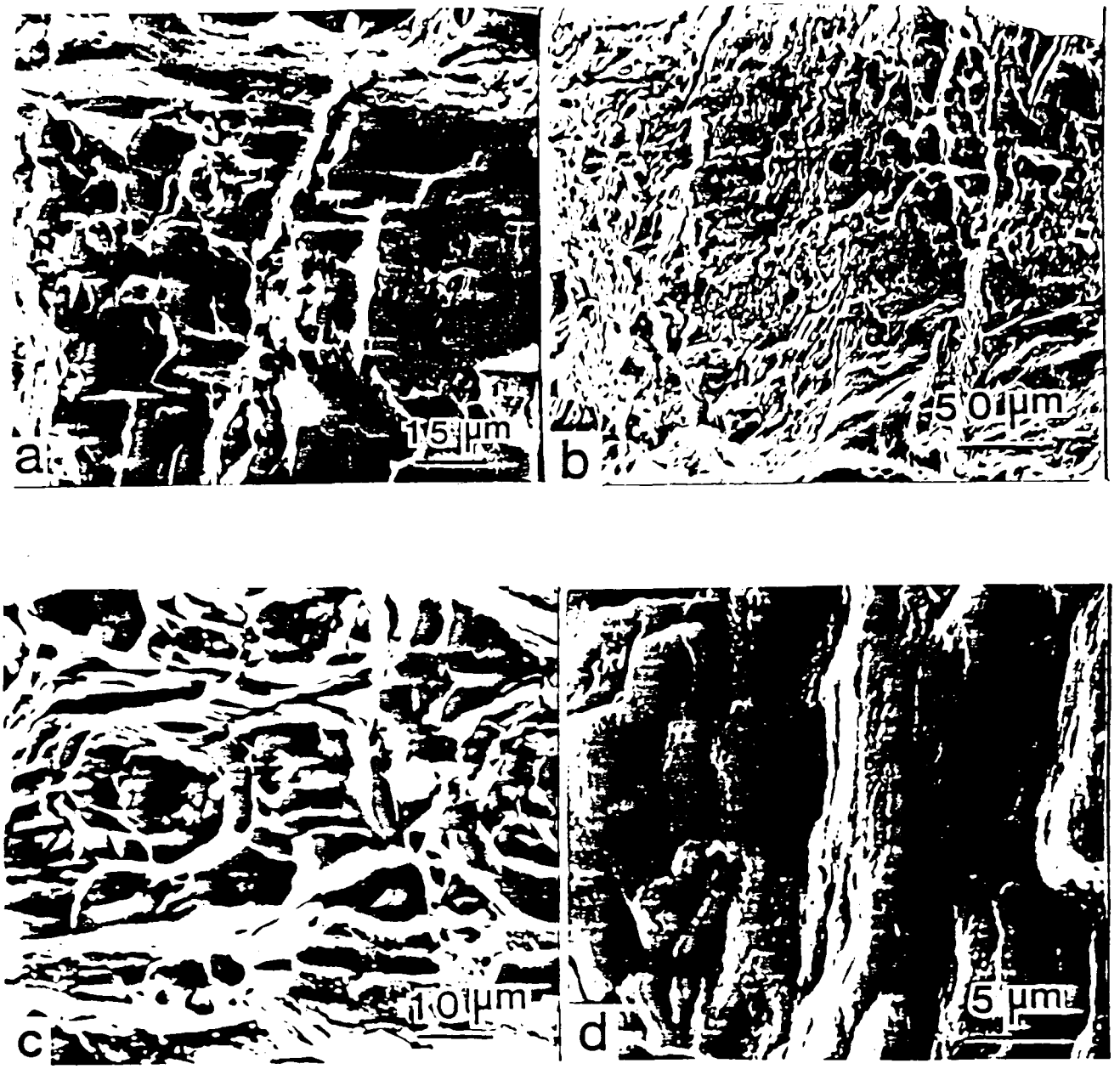

Figure 15: SEM micrographs of the fracture features in fracture toughness samples illustrating slip band fracture and secondary cracking (shown by arrow) in (a), LA-2 and (b) PA, microstructures, (c) rare occurrence of voids initiated at constituent particles, PA and (d) ductile intergranular and ductile inter-subgranular fracture in OA-2.

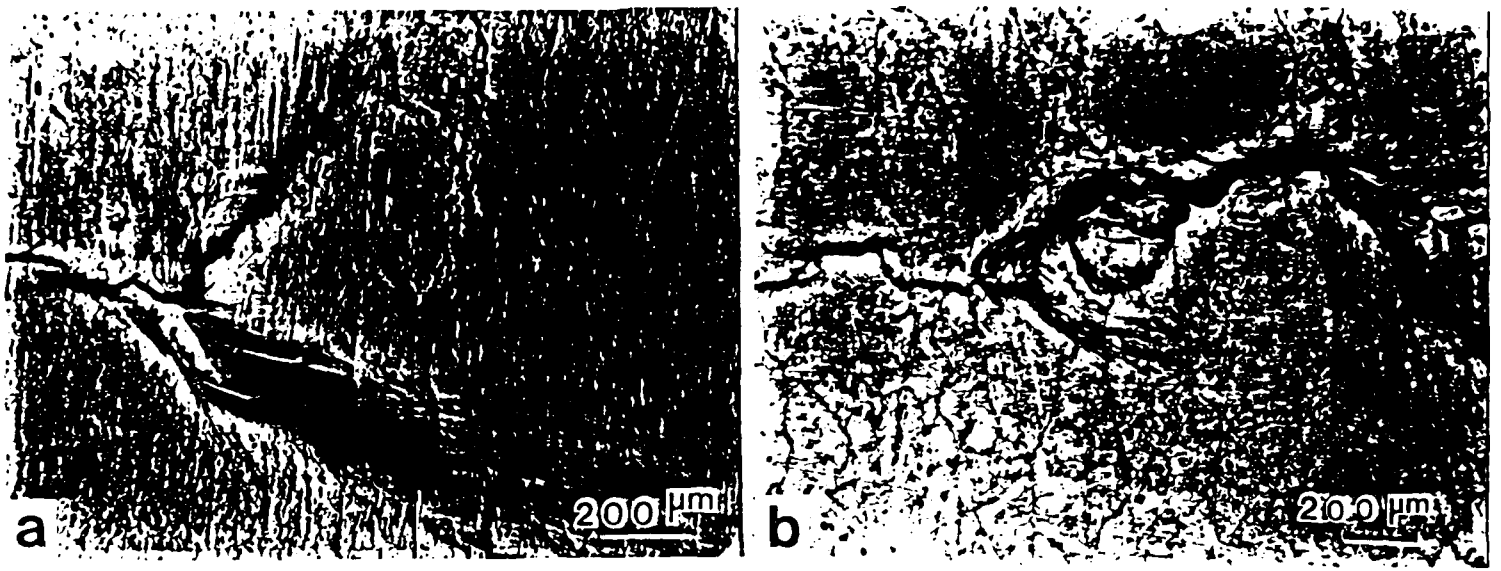

Figure 16: Optical micrographs comparing the plastic zones, taken after unloading at the onset of initial crack extension in (a) underaged, and (b) peakaged conditions.

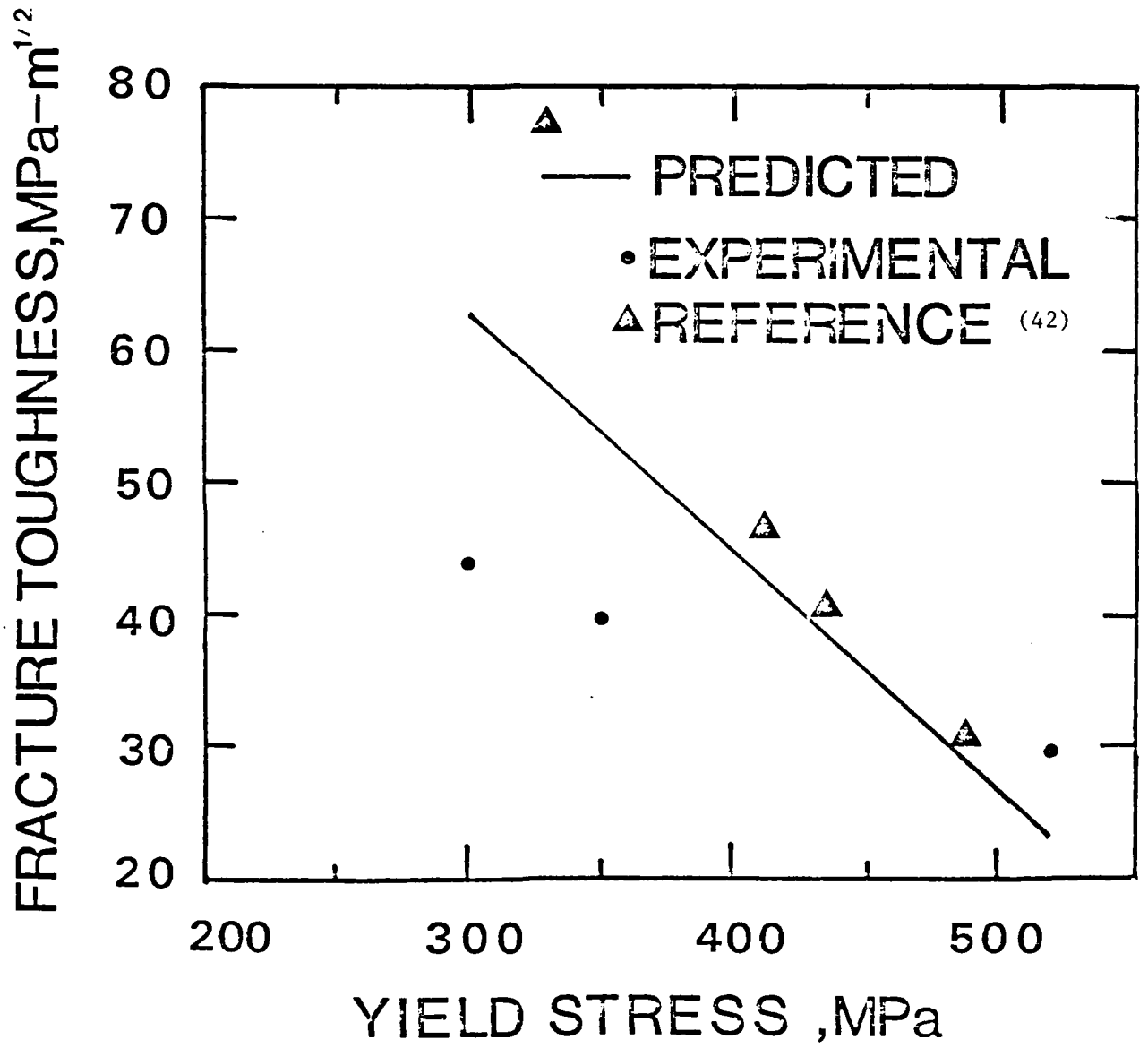

Figure 17: A comparison of the predicted fracture toughness values to the experimental values.

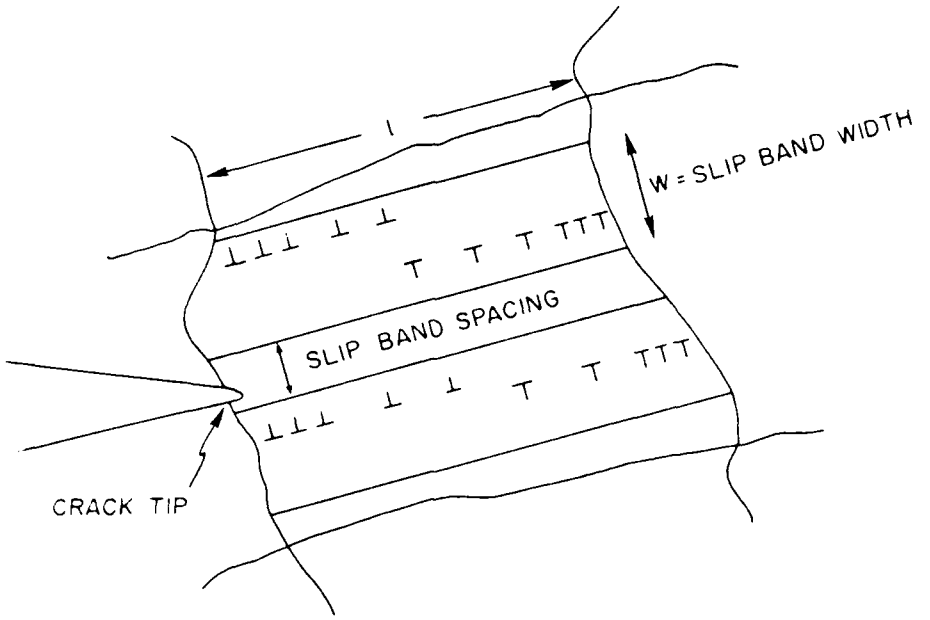

(a) UNDERAGED

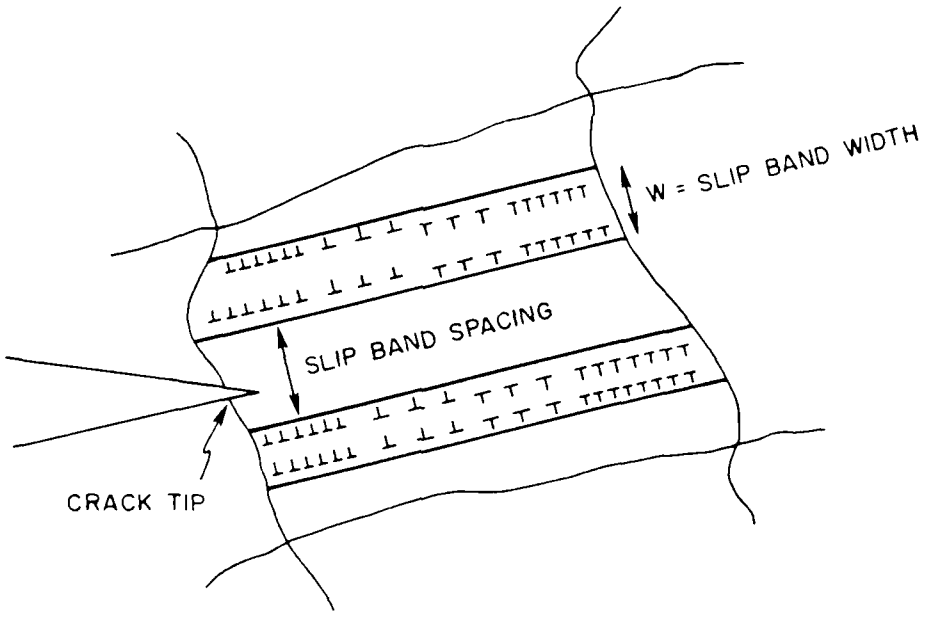

(b) PEAKAGED

Figure 18: A schematic illustrating that the slip bands developed in front of the crack tip are wider and closed spaced in (a) underaged conditions due to less heterogeneous slip character and (b) narrower and widely spaced in the peakaged condition, due to more localized slip.

TASK III: SECONDARY CRACKING IN Al-Li-Cu, Al-Li-Mg AND Al-Li-Cu-Mg ALLOYS

P. Bourgasser, J. A. Wert, and E. A. Starke, Jr.

Introduction

Task III of the research conducted on this program during 1985 addressed a topic of critical importance for application of Al-Li-base alloys in plate and extrusion form. Many recent studies of Al-Li-Cu and Al-Li-Cu-Mg alloys have shown that these alloys can exhibit severe grain boundary cracking [1-8]. The most commonly-observed manifestation of this grain boundary cracking is appearance of secondary cracks on fracture surfaces of tensile specimens loaded parallel to the rolling direction. In addition, studies of tensile properties in the short transverse orientation have demonstrated the deleterious effect of grain boundary fracture on short transverse ductility. This phenomenon is of relatively minor importance in sheet products because sheet is rarely loaded in the short transverse direction. However, plate and extruded products are frequently loaded in the short transverse direction and poor grain boundary strength would be a limiting factor in some applications.

The grain boundary cracking phenomenon is particularly notable because Al-Li-base alloys of commercial compositions are usually unrecrystallized after hot rolling to final gauge. Consequently, the grains are large and become very elongated during hot rolling. It is not unusual to find an average grain intercept length larger than 1 mm in the longitudinal direction, as illustrated in Fig. 1. These long boundaries become planes of weakness when the material is loaded in the short transverse direction.

The fundamental question addressed by this part of the program is why grain boundary cracking occurs in Al-Li-base alloys. Once the origin of grain boundary weakness is understood, development of composition or processing

variations which can reduce or suppress this grain boundary cracking problem will be pursued.

We have identified four potential mechanisms which could give rise to grain boundary cracking in Al-Li-base alloys.

1. Modulus Effect

A lithium-depleted zone, about 1 micrometer wide, has been observed at grain boundaries in a binary Al-12.9 at% Li alloy [9]. Detection of such lithium depleted zones is difficult because Li cannot be detected by conventional energy dispersive X-ray systems. Electron energy loss spectroscopy (EELS) was used by Williams and Edington [9] to measure the depleted region in the binary Al-Li alloy. No additional measurements have been reported.

Since lithium has a strong influence on the elastic modulus of aluminum alloys (a 1 wt% addition of lithium leads to a 6% increase of the elastic modulus [10]), grain boundary regions depleted of lithium would have a lower elastic modulus. A variation of modulus adjacent to the grain boundary would have the effect of concentrating stresses in the vicinity of the boundary, potentially causing premature failure in the low modulus layers adjacent to the boundary.

If this explanation is correct, a new processing method is an attractive candidate solution. Synthesis of heat treatments to reduce the extent of lithium depletion, or processing treatments to move boundaries away from lithium-depleted areas, both have the potential to eliminate the stress concentrations caused by lithium depletion at grain boundaries.

2. Segregation of Na or K to Grain Boundaries

Segregation of Na, Ca and K to grain boundaries has been shown to produce grain boundary weakness in aluminum alloys [4,5,11-15]. High grain

boundary concentrations of Na and K have been found in two Al-Li-base alloys which exhibited intergranular fracture. A study by Vasudevan and coworkers at ALCOA [5] concentrated on a binary Al-Li alloy to which deliberate additions of Na were made. Underaged treatments showed a strong effect of Na concentration which promoted intergranular fracture. Overaged treatments were universally brittle, an effect due to strain localization during deformation. Thus, Na did not have a strong effect on ductility and toughness of overaged alloys which were embrittled by an alternate mechanism. The alloys examined by Vasudevan and coworkers [5] were completely recrystallized.

A second study, carried out by Wert and Lumsden at Rockwell International [4], focused on an unrecrystallized Al-Li-Cu-Mg-Zr alloy of near-commercial composition. High concentrations of K were found on intergranular fracture surfaces by scanning Auger microscopy. Although K levels could not be varied in this commercial-type alloy, previous studies have associated K with grain boundary weakness in Al alloys [4,5,11-15]. Thus, segregation of K to grain boundaries in the alloy studied by Wert and Lumsden strongly implicates K as a grain boundary weakening agent in complex alloys with compositions near those of evolving commercial alloys.

Originally, Na and K were thought to be introduced into Al-Li-base alloys as impurities in the lithium addition. However, it is now believed that these impurities come from partial dissolution of refractory furnace liners by Al-Li-base alloys. Molten Al-Li-base alloys are very aggressive and react more strongly with refractories than other commercial-type aluminum alloys. Consequently, elimination of the source of Na and K contamination does not appear feasible. Melt treatments designed to lower Na and K levels are apparently available and may be able to reduce the level of Na and K contamination to lower levels. However, in unrecrystallized alloys, grain

boundaries remain in locations where Na and K segregate during solidification. Consequently, even low contamination levels may produce grain boundary weakness in unrecrystallized alloys.

Thermomechanical processing treatments designed to provoke recrystallization, thus moving grain boundaries away from locations of high Na and K contamination appear to offer a potential solution to the problems caused by presence of these impurity elements. Such treatments will be investigated in this research program.

3. Grain Boundary Precipitation

Large equilibrium phase particles often precipitate at grain boundaries in Al-Li-base alloys, as in most heat-treatable aluminum alloys. Vasudevan and coworkers at ALCOA [8] have reported that intergranular fracture is due to the presence of these particles. Evidence for this conclusion was derived from comparative experiments on Al-Li alloys containing Al_3Li particles and Ni-base superalloys containing Ni_3Al particles. The crystal structure of Al_3Li and Ni_3Al are identical and both matrices have fcc crystal structures. However, Ni_3Al is the equilibrium phase in superalloys and thus no grain boundary precipitates form. Comparison of the fracture characteristics of these alloys led Vasudevan and coworkers [8] to conclude that grain boundary precipitation of equilibrium phases is the cause of grain boundary weakness in Al-Li-base alloys.

The concepts used by Vasudevan and coworkers [8] are extremely useful, but comparison of Al-base and Ni-base alloy characteristics presents several difficulties. For example, Ni-base alloys are not prone to grain boundary weakness caused by impurities such as Na and K. Moreover, characteristics such as stacking fault energy, antiphase boundary energy, precipitate misfit, average particle size and coherent particle interfacial

energy; which may profoundly influence the course of deformation and fracture; are not the same in these two alloy classes. A more conclusive experiment would be possible with an Al-Li-base alloy in which the Al_3Li phase was stabilized to become the equilibrium phase. In this case, grain boundary precipitation of AlLi phase would be eliminated and a direct comparison between the two aluminum alloys would be feasible. Such an experiment is included in a proposal prepared by the University of Virginia for the Naval - Air Development Center. Results from that program are expected to permit careful assessment of the role of grain boundary AlLi precipitation on intergranular fracture.

4. Strain Localization

Strain localization has been shown to produce intergranular fracture in binary Al-Li alloys where precipitate shearing leads to concentration of slip into intense bands. Intersection of these slip bands with grain boundaries initiates intergranular fracture at relatively low strain levels [15]. Addition of Cu and Mg to Al-Li alloys is the currently-accepted method for reducing the strain localization problem caused by high volume fractions of shearable Al_3Li particles. Although ductility is markedly increased by Cu and Mg additions, intergranular fracture is still observed. Since strain localization occurs to some extent in all precipitation-hardening aluminum alloys, but other alloys do not display intergranular fracture of the type exhibited by Al-Li-base alloys, it seems unlikely that strain localization alone could account for the observations of intergranular fracture in commercial-type Al-Li-Cu-(Mg) alloys.

A second possible mechanism of strain localization is concentration of strain in the PFZs along grain boundaries [15]. However, stretching before aging is a classic method for eliminating PFZs through introduction of

nucleation sites for intermediate precipitates. Many studies have shown that stretching improves longitudinal ductility of Al-Li alloys [1,2,4,16], and TEM investigations have shown that PFZs are substantially eliminated by the stretching treatment. However, no effect of stretching was found on short transverse ductility [4], nor did stretching eliminate the occurrence of intergranular cracks on longitudinal tensile fracture surfaces. Thus we conclude that strain localization due to PFZs is not the primary cause of the intergranular cracking phenomenon observed in Al-Li-base alloys of near-commercial composition.

Research Objectives

This research program is designed to assess the importance of candidate mechanisms 1 through 4 listed above. Additional results from other programs currently being conducted at the University of Virginia will add support to the conclusions of the present program. It is our intention to address the fundamental questions:

1. What is the origin of intergranular fracture in commercial-type Al-Li-Cu-(Mg) alloys?
2. What can be done to reduce or eliminate this type of fracture?

Each of the potential mechanisms of intergranular fracture poses a set of intermediate questions which must be addressed to uncover the final answers to the primary questions listed above.

Technical Progress

Investigation of two Al-Li-Cu-(Mg) alloys has been underway for a 3-month period at the end of the present reporting period (1985), and will continue in 1986. During the initial 3 months of this research effort, we have focused on characterizing the alloys:

- Two alloy compositions were selected.
- An understanding of the microstructure and how it evolved during processing has been established.
- Bulk chemical composition has been related to the potential grain boundary composition of impurities.
- TEM characterization of grain boundary precipitation has been conducted.
- X-ray pole figures were determined.

Two alloys, designated as LC1 and LCM1, are presently being investigated. They were cast and hot-rolled to 12.7 mm plate by Reynolds Metals Co. The alloys were DC cast in the form of ingots with a 168 mm x 81 mm cross-section. After casting, they were homogenized 24 hrs at 543°C and hot rolled to 12.7 mm thick plate, which represents an 84% reduction ratio. Cross-rolling was used during initial break-down of the ingots, to provide a final plate of the desired dimensions. Reynolds Metals Co. also supplied pieces of the ingots, which permitted characterization of the as-cast structure and of changes that occurred in the structure during hot rolling.

The result of the chemical analysis of these two alloys, performed by Luvak Inc., is given in Table 1.

Table 1

Alloy Composition (Wt %)

	LC1	LCM1
Li	2.45	2.46
Cu	2.43	2.04
Mg	.003	.96
Zr	.18	.14
Fe	.098	.11
Si	.089	.047
Na	.0014	.0006
K	.0005	.0005
Ca	<.0005	<.0005

According to the International Aluminum Association code, LC1 is a 2090-type alloy, and LCM1 is an 8091-type alloy. ALCAN International will commercialize the 8090 and 8091 alloy compositions and ALCOA will commercialize the 2090-type alloys.

1. Metallographic Study

The purpose of this study was to characterize the grain structure of the alloys, and to determine the appropriate solution heat treatment temperature for these alloys.

Samples of both alloys were first solutionized in a salt bath at 530°C for 15 min. Keller's reagent was used to etch the samples, permitting observation of the grain structure. In both alloys, the grains had the familiar pancake morphology. Fig. 1 shows the microstructures in all three orientations. A substantial difference in the size of the grains was found for the two alloys, the Mg-containing alloy having a coarser grain structure. Mean linear intercept grain sizes are given in Table 2.

Table 2

Grain Size of Hot-Rolled Plate

Alloy	L-direction μm	T-direction μm	S-direction μm
LC1	300-400	100-200	20-60
LCM1	400-1000	200-400	40-100

Some particles, identified as undissolved precipitates, were observed after solution treatment at 530°C. Studies at Reynolds Metals Co. and at the University of Virginia have shown that 530°C does not produce maximum precipitation hardening, confirming that solution treatment at 530°C results in incomplete solution of the precipitating phases. Additional specimens were solution heat treated at 550°C for periods of 15 min., 30 min. and 1 hour in an effort to determine appropriate solution heat treatment temperature and time. Results of these studies showed that solution treatment for 15 min. or longer at 550°C completely dissolves soluble precipitates. Consequently, a solution heat treatment at 550°C during 30 min. was chosen for the following experiments.

In addition to determining grain morphology and appropriate solution treatment temperatures, metallographic study of the microstructure of the cast material provided insight into the evolution of microstructure during processing. Figs. 2a and 2b shows the cast microstructures before homogenization, the plane of the photographs is normal to the casting direction and the location is approximately at the center of the section. Little difference was found in grain size from the edge to the center of the castings. These cast structures are typical of grain-refined, DC-cast aluminum alloys. The cast grain size cannot be determined from these photographs because the grains do not have sufficient contrast. Additional

micrographs, shown in Figs. 2c and 2d, were taken following anodizing. These results allowed the grain sizes in the castings to be determined.

Knowing the cast grain size and the extent of reduction, the final grain size can be calculated assuming no recrystallization during hot rolling. Results of these calculations are shown in Table 3. The calculated and measured short transverse grain sizes compare favorably, leading us to conclude that recrystallization did not occur during hot rolling. This conclusion is supported by the X-ray results presented in the following section.

Table 3

Prediction of Grain Size After Hot Rolling

As-Cast Alloy	μm	Hot-Rolled Predicted μm	Hot-Rolled Observed μm
LC1	83.8	13.1	18.5
LCM1	287	44.8	40.0

A surprising feature of the cast structures is the difference in dendrite spacing and grain structure in two nominally-identical castings. Dendrite spacing is usually controlled by cooling rate, the difference in structure thus suggests a rather large difference in cooling rate of these two alloys. However, Reynolds Metals Co., producer of this material, is confident that the cooling rates were approximately equal for these two castings. The origin of the grain size difference is not presently known. Although the grain size of the casting is reflected in the hot-rolled microstructure, this difference is not thought to pose substantial problems in interpreting the results of the present study.

2. X-ray Investigation

Since this study is addressing fracture at grain boundaries, it is essential to determine whether these alloys recrystallized during hot rolling or during the solution heat treatment at 550°C. Metallographic investigation showed the grains to be large and elongated in the longitudinal and long transverse directions. This grain morphology could be characteristic of either:

- unrecrystallized grains, in which case the grain size and aspect ratio would be related to the original cast grain size and to the degree of rolling reduction, or
- recrystallized grains which are usually elongated in aluminum alloys due to preferential growth during recrystallization.

Pinhole back reflection patterns and pole figures were measured to determine the extent of recrystallization during hot rolling.

Samples of both alloys were solution heat treated, mechanically polished (600 grit), etched 2 min. in sodium hydroxide at 70°C and cleaned in dilute nitric acid before pole figure determination was performed. The same samples were used for pinhole back-reflection experiments.

The [111] pole figures for both alloys, shown in Fig. 3, are typical of rolled aluminum alloys. Evidence of cross-rolling during hot rolling of the ingots can be seen in the pole figures. The pole figures support the conclusion that no recrystallization occurred during the final rolling steps or during subsequent solution treatment. Pinhole back-reflection photographs showed essentially continuous rings rather than individual reflections, confirming the presence of a deformation substructure in both alloys.

3. Transmission Electron Microscopy

Both alloys are being characterized by TEM to establish their grain, sub-grain and precipitation structure. The presence of stable phases at the grain boundaries was also examined in detail. So far, only solution-treated alloys have been characterized using TEM. Thin foils from the L-T section of the materials were obtained by mechanical polishing and subsequently electro-polishing in a 3:1 methanol:nitric solution at -15°C.

The elongated grain structure found by optical microscopy was also evidenced in the TEM specimens. In addition, a subgrain boundary network was observed within the elongated grains, with an average subgrain diameter of about one third of the short-transverse grain dimension. This subgrain structure, also found by previous investigators in similar alloys [16], is the result of recovery during hot rolling.

The main focus of our TEM study is characterization of particles at grain boundaries and subgrain boundaries. Results obtained during the initial period of investigation have led to the following conclusions:

Subgrain boundaries are free of particles after solution treatment. Thus, any particles observed on subgrain boundaries after aging must be soluble particles precipitated during aging.

Grain boundaries have a significant particle population after solution treatment. These particles are fairly large and are either globular or lenticular, in which case they are usually aligned in the rolling direction. These particles are generally too large to permit selected area diffraction patterns to be obtained. Thus, the primary means of identification of these particles will be micro-EDS using the STEM. Preliminary analysis has revealed that some of the particles contain Si in combination with other elements, but detailed characterization is underway.

Grain interiors have been found to contain Al_3Li, Al_3Zr and constituent particles similar to those found at grain boundaries. The dispersion of Al Li was very fine in the unaged samples, as is expected for precipitates that form during quenching. The inability to suppress Al_3Li by conventional quenching procedures has been noted by previous investigators [16]. The Al_3Zr particles were found to have an average diameter of 7 nm, typical of many other aluminum alloys containing Zr. The density of constituent particles found in grain interiors was quite low, the majority of these particles being concentrated at grain boundaries. However, no systematic differences in particle size or morphology have been observed between the constituent particles at grain boundaries and in grain interiors.

4. Tensile Test Results

Limited tensile testing of aged samples has shown that the two alloys selected for this study do indeed exhibit the intergranular fracture behavior being studied. Fig. 4 shows a fractograph of alloy LCM1 solution treated at 550°C for 30 minutes, quenched and aged at 190°C for 48 hours. A complete description of the tensile results will be incorporated into a subsequent report.

Tasks Planned for 1986

We envision that the following tasks will be carried-out during the next year to identify the factor(s) that contribute to intergranular fracture in the two Al-Li-base alloys under investigation.

Tensile Tests. Full characterization of the tensile properties will be completed with the goal of delineating the effects of aging treatment on the severity of intergranular fracture. Extensive fractography will be conducted with the failed tensile specimens. In addition, short transverse tensile tests may be conducted to provide specimens which will allow the topology of

the intergranular fracture to be characterized. This is expected to aid in assessing the role of grain boundary precipitates in the intergranular fracture process. Characterization of grain boundaries fractured by liquid metal embrittlement will permit the effect of plastic deformation on the fracture topology to be assessed.

TEM. A more complete analysis of the grain boundary regions will be carried out, with emphasis on identifying the composition of the grain boundary constituent particles. In addition, TEM analysis of slightly deformed specimens will be used to determine if concentration of strain occurs in the vicinity of the grain boundaries. Such strain concentrations could be caused by modulus variations, by PFZs or by the stress concentrating effects of grain boundary particles.

Thermomechanical Processing. Movement of boundaries away from locations where constituent particles or impurities such as Na and K have concentrated may dramatically improve the short transverse ductility. Although Al-Li-base alloys containing Zr are difficult to recrystallize, processing techniques such as those developed under AFOSR sponsorship at Rockwell International are suitable for provoking recrystallization in these alloys. Tensile tests conducted before and after such processing will establish the value of thermomechanical processing treatments for alleviation of the intergranular fracture problem, and will aid in identifying the cause of this problem.

Modeling. Modeling of the stress concentration which could be caused by the variation in modulus will permit the importance of this potential source of intergranular fracture to be assessed. Since the variation of elastic modulus with lithium concentration and the lithium concentration profile at the grain boundaries is known, modeling can be conducted without further experimental information.

Auger Analysis. If the thermomechanical processing results suggest that boundaries are indeed moved away from regions where impurities or constituent particles may be concentrated, we may find that Auger analysis of the original boundaries is required to assess the concentration of Na or K in the original boundary locations. Arrangements will be made to use the facilities at Oak Ridge National Laboratory for these analyses.

References

1. F. S. Lin, S. B. Chakrabortty and E. A. Starke, Jr., Met. Trans., 13A (1982) 401.

2. R. E. Crooks and E. A. Starke, Jr., Met. Trans., 15A (1984) 1367.

3. E. A. Starke, Jr. and F. S. Lin, Met. Trans., 13A (1982) 2259.

4. J. A. Wert and J. B. Lumsden, Scripta Met., 19 (1985) 205.

5. A. K. Vasudevan, A. C. Miller and M. M. Kersker, in Aluminum Lithium Alloys II, T. H. Sanders, Jr. and E. A. Starke, Jr. (eds.), TMS-AIME, Warrendale, PA, 1983, p.181.

6. R. J. Kar, J. W. Bohlen and G. R. Chanani, in Aluminum Lithium Alloys II, T. H. Sanders, Jr. and E. A. Starke, Jr. (eds.), TMS-AIME, Warrendale, PA, 1983, p.181.

7. W. S. Miller, M. P. Thomas, D. J. Lloyd and D. Creber, in Aluminum Lithium Alloys II, The Institute of Metals, in press.

8. A. K. Vasudevan, E. A. Ludwiczak, S. F. Baumann, R. D. Doherty and M. M. Kersker, in Aluminum Lithium Alloys II, The Institute of Metals, in press.

9. D. B. Williams and J. W. Edington, Phil. Mag., 30 (1974) 1147.

10. E. A. Starke, Jr., in Sixth International Conference on the Strength of Metals and Alloys, R.C. Gifkins (ed), Pergamon Press, Oxford, (1983), 1025.

11. C. E. Ransley and D. E. J. Talbot, J. Inst. Metals, 88 (1959-60) 150.

12. J. W. Evancho, NAVAIR Contract No. 62269-73-C-0219, Final Report, June 1974.

13. Y. M. Vaynblat, B. A. Kopeliovich and Y. G. Gol'der, Physics of Metals and Metallography, 42 (1976) 105.

14. T. H. Sanders, Jr., NAVAIR Contract No. N62269-76-C-0271, Final Report, June 1979.

15. E. A. Starke, Jr., T. H. Sanders, Jr. and I. G. Palmer, Journal of Metals, 33 (1981) 24.

16. Aluminum Lithium Alloys II, T. H. Sanders, Jr. and E. A. Starke, Jr. (eds.), TMS-AIME, Warrendale, PA, 1983, p.181.

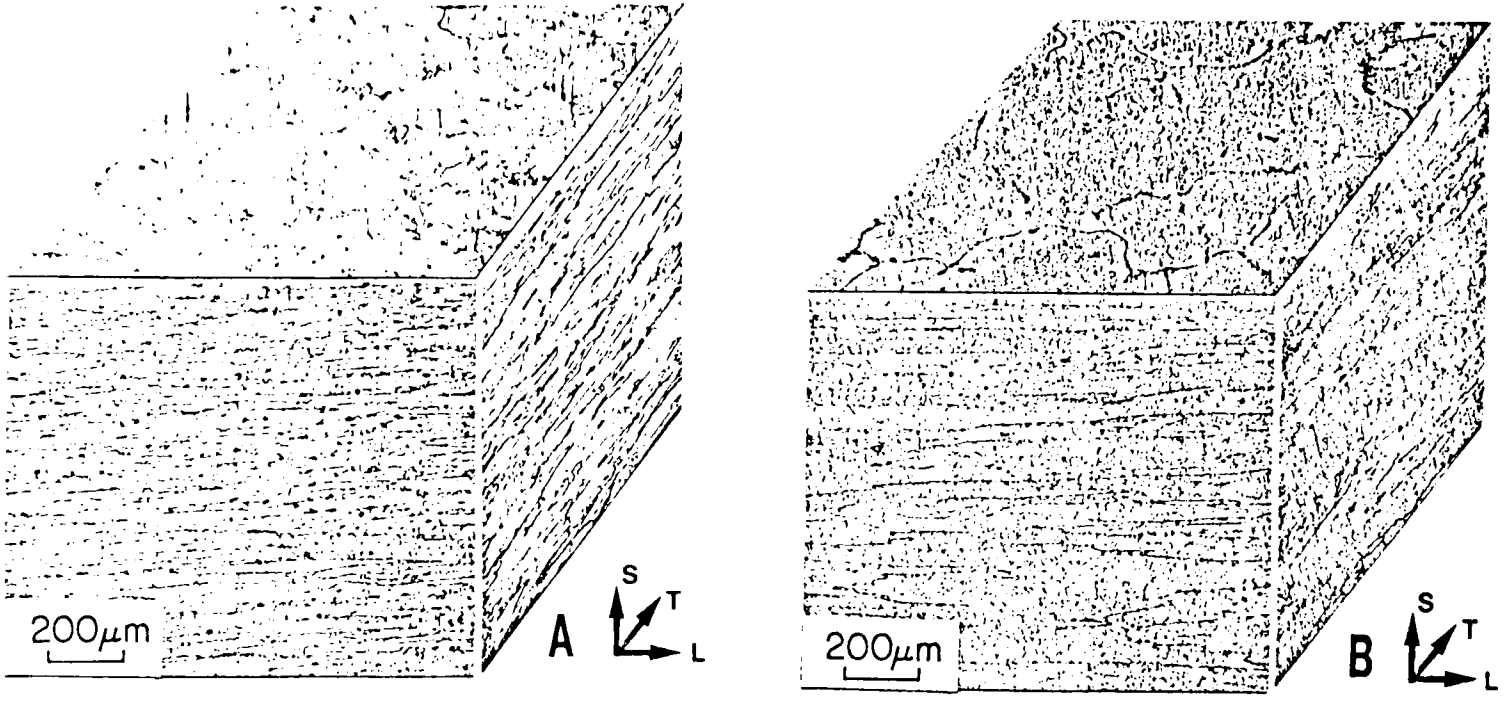

Figure 1. Grain morphology after hot rolling of Al-Li-Cu-(Mg)-Zr alloys under investigation in Part 3 of this program. A: Alloy LC1. B: Alloy LCM1.

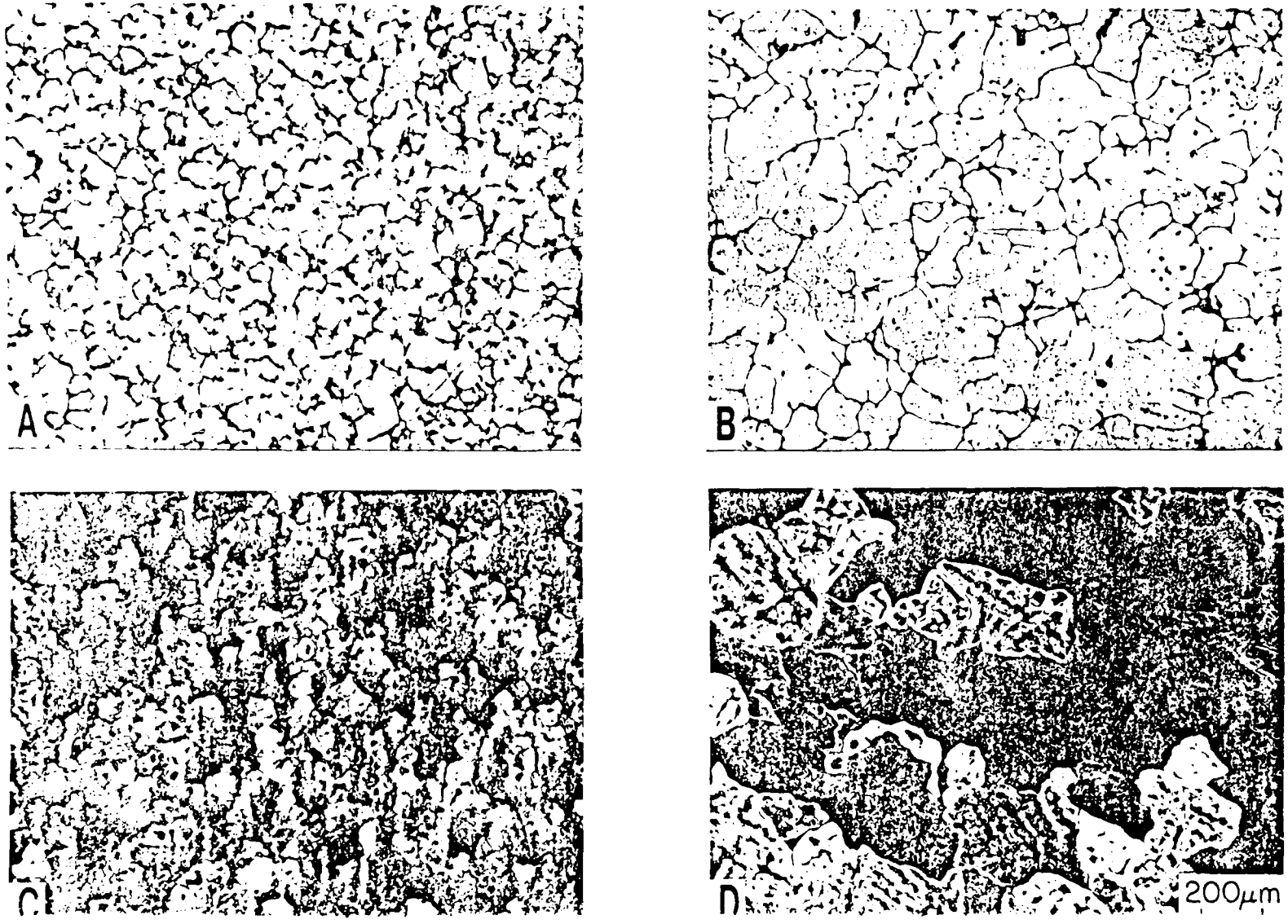

Figure 2. As-cast grain morphology of Al-Li-Cu-(Mg)-Zr alloys under investigation in Part 3 of this program. Upper micrographs show dendritic structre, lower micrographs show cast grain morphology. A and C: Alloy LC1. B and D: Alloy LCM1.

AD-A170 136 THE USE OF NOVEL PROCESSING PROCEDURES FOR IMPROVING 2/2
OVERALL FATIGUE RESI. (U) VIRGINIA UNIV CHARLOTTESVILLE
DEPT OF MATERIALS SCIENCE E A STARKE APR 86
UNCLASSIFIED UVA/525644/MS86/101 AFOSR-TR-86-0492 F/G 11/6 NL

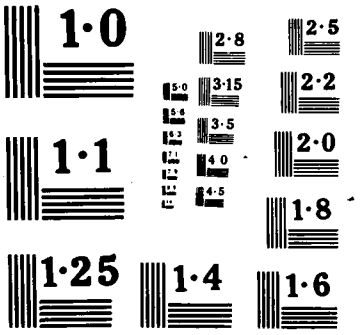
1·0
1·1
1·25
1·4
1·6
1·8
2·0
2·2
2·5
2·8
3·15
3·5
4·0
4·5
5·0

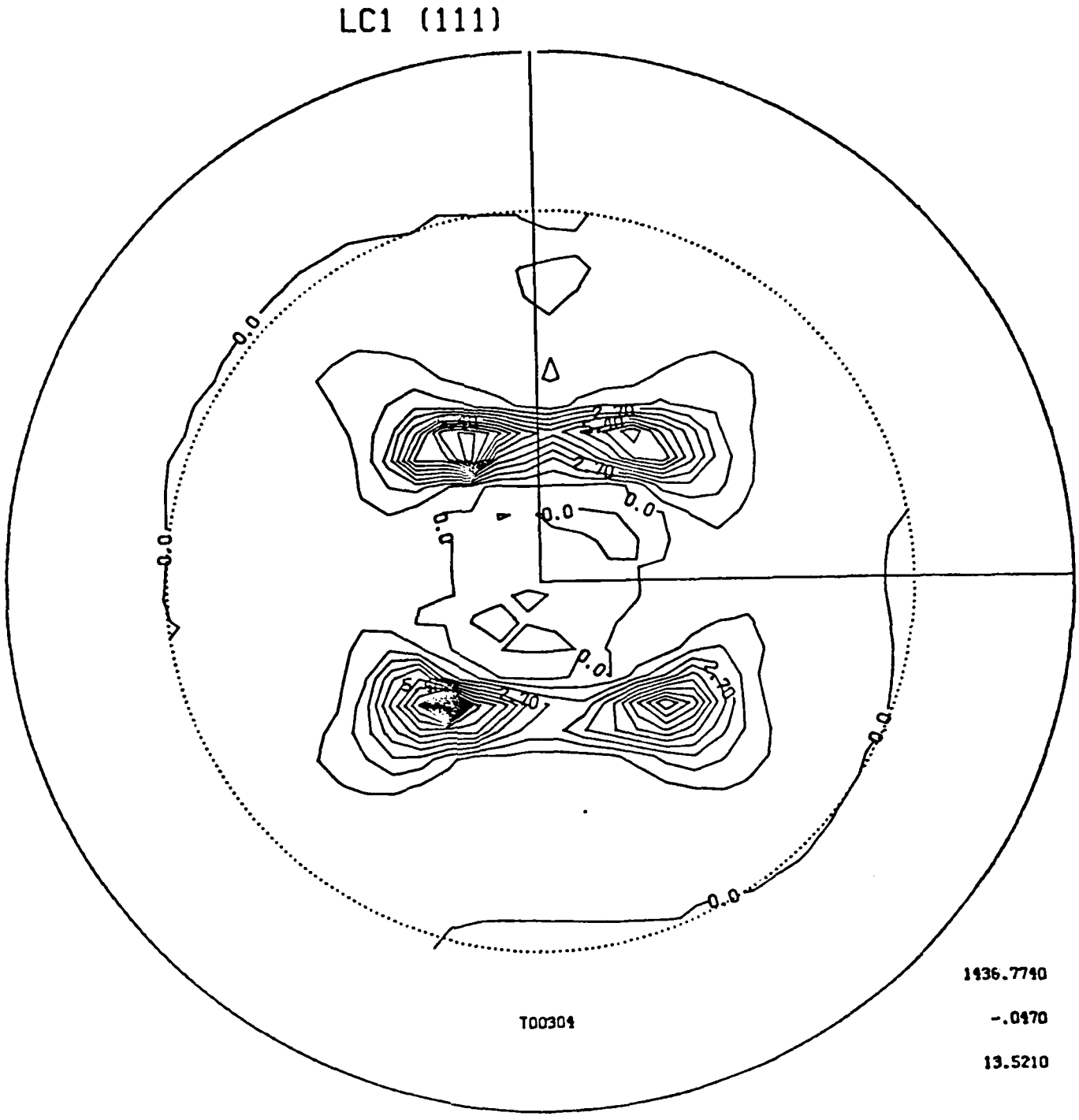

Figure 3a. Alloy LC1. [111] pole figures of hot rolled Al-Li-Cu-(Mg)-Zr alloys under investigation in Part 3 of this program.

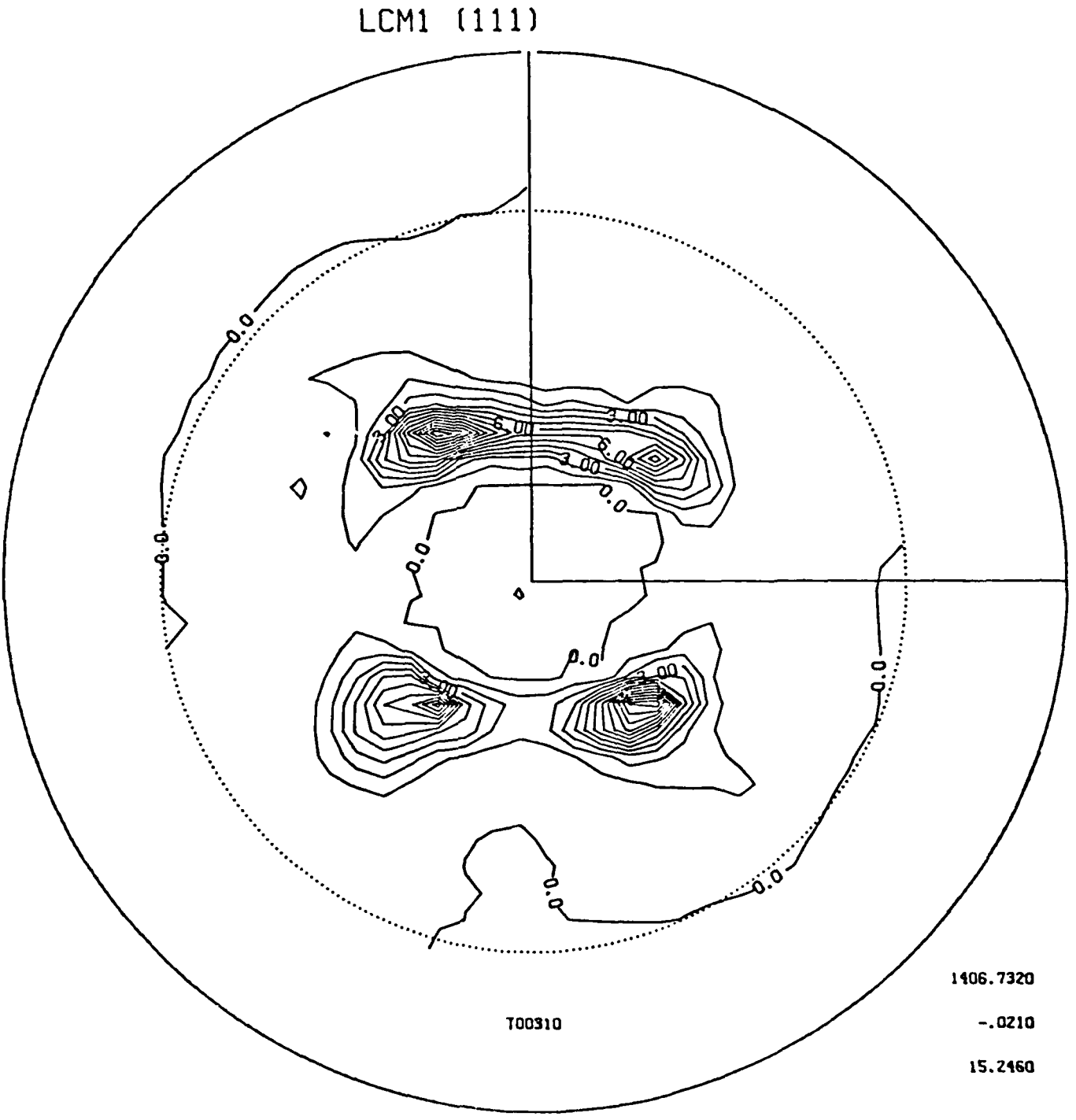

Figure 3b. Alloy LCM1. [111] pole figures of hot rolled Al-Li-Cu-(Mg)-Zr alloys under investigation in Part 3 of this program.

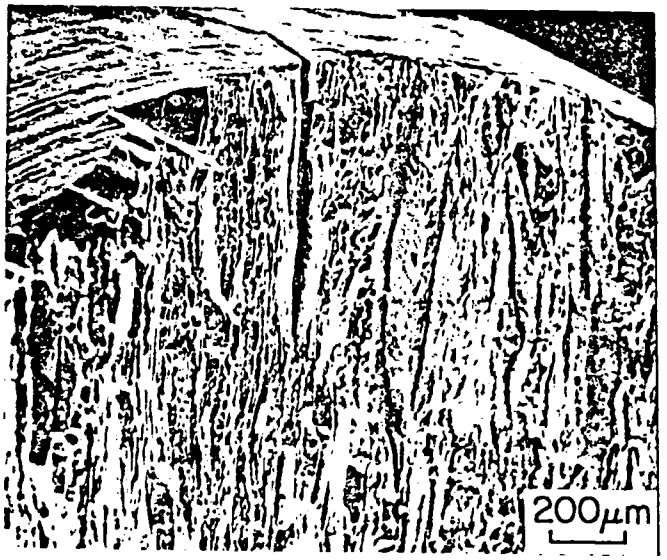

Figure 4. Fractograph of alloy LCM1 solution treated at 550°C for 30 minutes, quenched and aged at 190°C for 48 hours.

PROFESSIONAL PERSONNEL

Dr. Edgar A. Starke, Jr., Principal Investigator
Dr. John A. Wert
Dr. Kumar V. Jata
Dr. Wolfgang Ruch
Dr. Mark Duva

GRADUATE STUDENTS

Pascal Bourgasser

PRESENTATIONS

1. K.V. Jata and E.A. Starke, Jr., "Fatigue Crack Growth and Fracture Toughness Behavior of an Al-Li-Cu Alloy," Third International Aluminum-Lithium Conference, Oxford, England, July 8-11, 1985.

2. F.G. Daus, K.V. Jata and E.A. Starke, Jr., "The Effect of Manganese-Dispersoid Content on Strain Hardening and Fracture Toughness in a Very Pure Al-Cu-Mg Alloy," TMS-AIME Fall Meeting, Toronto, Canada, October 13-17, 1985.

3. Kumar V. Jata, Wolfgang Ruch, and Edgar A. Starke, Jr., "The Fatigue and Fracture Behavior of Al-Li-X Alloys Produced by Mechanical Alloying and Ingot Metallurgy Methods," European Materials Research Society Symposium on Light Metals, Strasbourg, France, November 26-28, 1985.

PUBLICATIONS

1. K.V. Jata and E.A. Starke, Jr., "Fatigue Crack Growth and Fracture Toughness Behavior," Met. Trans. A. (in press).

2. K.V. Jata and E.A. Starke, Jr., "Fatigue Crack Growth and Fracture Toughness Behavior of an Al-Li-Cu Alloy," Aluminum-Lithium Alloys III, C. Baker, P.J. Gregson, S.J. Harris and C.J. Peel, eds., The Institute of Metals, London, 1986, 247-256.

3. Kumar V. Jata, Wolfgang Ruch, and Edgar A. Starke, Jr., "The Fatigue and Fracture Behavior of Al-Li-X Alloys Produced by Mechanical Alloying and Ingot Metallurgy Methods," Proceedings of the European Materials Research Society Symposium on Light Metals, Strasbourg, France, November 26-28, 1985 (in press).

DISTRIBUTION LIST

Copy No.	
1 - 6	Air Force Office of Scientific Research/NE Building 410 Bolling Air Force Base Washington, D.C. 20332 Attention: Alan H. Rosenstein
7 - 8	E. A. Starke, Jr.
9 - 10	J. A. Wert, MS
11	K. R. Lawless, MS
12 - 13	E. H. Pancake/Clark Hall
14	SEAS Publications Files

JO# 7354:lsl

UNIVERSITY OF VIRGINIA
School of Engineering and Applied Science

The University of Virginia's School of Engineering and Applied Science has an undergraduate enrollment of approximately 1,500 students with a graduate enrollment of approximately 560. There are 150 faculty members, a majority of whom conduct research in addition to teaching.

Research is a vital part of the educational program and interests parallel academic specialties. These range from the classical engineering disciplines of Chemical, Civil, Electrical, and Mechanical and Aerospace to newer, more specialized fields of Biomedical Engineering, Systems Engineering, Materials Science, Nuclear Engineering and Engineering Physics, Applied Mathematics and Computer Science. Within these disciplines there are well equipped laboratories for conducting highly specialized research. All departments offer the doctorate; Biomedical and Materials Science grant only graduate degrees. In addition, courses in the humanities are offered within the School.

The University of Virginia (which includes approximately 2,000 faculty and a total of full-time student enrollment of about 16,400), also offers professional degrees under the schools of Architecture, Law, Medicine, Nursing, Commerce, Business Administration, and Education. In addition, the College of Arts and Sciences houses departments of Mathematics, Physics, Chemistry and others relevant to the engineering research program. The School of Engineering and Applied Science is an integral part of this University community which provides opportunities for interdisciplinary work in pursuit of the basic goals of education, research, and public service.

END

DTIC

9-86